Article

Calcium-Voltage Coupling in the Genesis of Early and Delayed Afterdepolarizations in Cardiac Myocytes

Zhen Song,[1,2] Christopher Y. Ko,[1,2] Michael Nivala,[1,2] James N. Weiss,[1,2,3] and Zhilin Qu[1,2,*]
[1]Cardiovascular Research Laboratory, [2]Department of Medicine (Cardiology), and [3]Department of Physiology, David Geffen School of Medicine, University of California, Los Angeles, California

ABSTRACT Early afterdepolarizations (EADs) and delayed afterdepolarizations (DADs) are voltage oscillations known to cause cardiac arrhythmias. EADs are mainly driven by voltage oscillations in the repolarizing phase of the action potential (AP), while DADs are driven by spontaneous calcium (Ca) release during diastole. Because voltage and Ca are bidirectionally coupled, they modulate each other's behaviors, and new AP and Ca cycling dynamics can emerge from this coupling. In this study, we performed computer simulations using an AP model with detailed spatiotemporal Ca cycling incorporating stochastic openings of Ca channels and ryanodine receptors to investigate the effects of Ca-voltage coupling on EAD and DAD dynamics. Simulations were complemented by experiments in mouse ventricular myocytes. We show that: 1) alteration of the Ca transient due to increased ryanodine receptor leakiness and/or sarco/endoplasmic reticulum Ca ATPase activity can either promote or suppress EADs due to the complex effects of Ca on ionic current properties; 2) spontaneous Ca waves also exhibit complex effects on EADs, but cannot induce EADs of significant amplitude without the participation of $I_{Ca,L}$; 3) lengthening AP duration and the occurrence of EADs promote DADs by increasing intracellular Ca loading, and two mechanisms of DADs are identified, i.e., Ca-wave-dependent and Ca-wave-independent; and 4) Ca-voltage coupling promotes complex EAD patterns such as EAD alternans that are not observed for solely voltage-driven EADs. In conclusion, Ca-voltage coupling combined with the nonlinear dynamical behaviors of voltage and Ca cycling play a key role in generating complex EAD and DAD dynamics observed experimentally in cardiac myocytes, whose mechanisms are complex but analyzable.

INTRODUCTION

Early afterdepolarizations (EADs) and delayed afterdepolarizations (DADs) are known to cause arrhythmias in a variety of cardiac diseases, including long QT syndromes (1–3), catecholaminergic polymorphic ventricular tachycardia (CPVT) (4,5), and heart failure (6,7). EADs are voltage oscillations that occur during the repolarizing phases of the action potential (AP). By prolonging the AP duration (APD) regionally, EADs can increase dispersion of refractoriness, forming a tissue substrate vulnerable to reentry. Furthermore, if EADs reach the threshold to propagate out this region as premature ventricular contractions, they can serve as triggers to induce reentry. DADs, on the other hand, are voltage oscillations during diastole. By depolarizing the resting membrane potential regionally, DADs can cause conduction block (8), and, if they reach the threshold for sodium (Na) channel activation, can generate triggered activity (TA) manifesting as premature ventricular contractions that induce reentry.

EADs occur in the setting of reduced repolarization reserve, such as long QT syndromes, and have classically been attributed to voltage-driven oscillations in the repolarizing phase of the AP, although spontaneous sarcoplasmic reticulum (SR) calcium (Ca) release has also been proposed as an important mechanism. DADs, on the other hand, are promoted by Ca cycling disorders, such as CPVT and digitalis toxicity, which promote Ca-driven oscillations. Heart failure represents a combination of reduced repolarization reserve and abnormal Ca cycling resulting from electrical and excitation-contraction coupling remodeling processes driven by both genetic transcriptional and posttranslational signaling components. In all of these settings, it is common for EADs and DADs to coexist and influence each other. This is because membrane voltage is strongly affected by Ca-sensitive ionic currents, and, conversely, cellular Ca loading is strongly influenced by voltage-dependent ionic currents, referred to as bidirectional Ca-voltage coupling. Ca-voltage coupling can promote complex AP dynamics in the heart (9). Analyzing the interactions between EADs and DADs (and voltage and Ca-cycling coupling dynamics in general), however, has been challenging, because the Ca cycling dynamics (e.g., Ca waves and oscillations) result from a spatially distributed heterogeneous network of Ca release units (CRUs) in the cell. The Ca waves emanating from various subcellular regions integrate to depolarize diastolic membrane voltage by activating Ca-sensitive inward currents including the Na-Ca exchange (NCX) current (I_{NCX}) and Ca-activated nonselective cation channels ($I_{ns(Ca)}$), generating DADs. Similarly, spontaneous SR Ca

Submitted October 29, 2014, and accepted for publication March 10, 2015.
*Correspondence: zqu@mednet.ucla.edu
Editor: Randall Rasmusson.

0006-3495/15/04/1908/14 $2.00
http://dx.doi.org/10.1016/j.bpj.2015.03.011

release during the AP plateau can potentially trigger EADs (10–13), in concert with voltage-dependent mechanisms generating voltage oscillations. Therefore, to analyze EAD and DAD dynamics realistically requires a detailed cardiac AP model incorporating spatiotemporal Ca cycling that can simulate Ca waves, such as the ones developed recently (14–16), rather than single pool models of Ca cycling.

In this study, we used our AP model incorporating detailed spatiotemporal Ca cycling in a network of diffusively-coupled CRUs to investigate systematically how bidirectional voltage-Ca coupling affects EAD and DAD dynamics. We show the following: 1) Alteration of the Ca transient can either promote or suppress EADs due to its complex effects on Ca-sensitive ionic currents. 2) Spontaneous Ca oscillations have complex effects on the occurrence and behavior of EADs, but cannot generate EADs of significant amplitude without the participation of $I_{Ca,L}$; the timing of a rise in intracellular Ca relative to membrane depolarization is not sufficient criteria to indicate that an EAD is caused by spontaneous SR Ca release. 3) Two different DAD mechanisms are identified (Ca-wave-independent and Ca-wave-dependent), and lengthening of APD promotes DADs by increasing intracellular Ca loading. The presence of EADs further enhances Ca loading to promote DADs due to more L-type Ca channel (LCC) openings during EADs. 4) Complex EAD patterns occur due to Ca-voltage coupling and are promoted under Ca overload conditions in both computer simulation and experiments of mouse ventricular myocytes. The mechanisms underlying these different EAD and DAD dynamics are analyzed and discussed.

MATERIALS AND METHODS

Computer model

The myocyte model contains a three-dimensional network of 19,305 (65 × 27 × 11) CRUs, modified from Restrepo et al. (14). Each CRU contains five subvolumes: network SR, junctional SR, dyadic space, submembrane space, and cytosolic space. Each CRU has a cluster of 100 ryanodine receptor (RyR) channels associated with a cluster of 12 LCCs, both simulated using random Markov transitions. The governing equation for voltage is

$$\frac{dV}{dt} = -\left(I_{Na} + \sum_{k=1}^{N\times m} i_{\mathrm{LCC}}(k) + I_{Ks} + I_{Kr} + \sum_{k=1}^{N} i_{\mathrm{NCX}}(k) + I_{\mathrm{NaK}} + I_{K1} + I_{to,f} + I_{to,s}\right) \Big/ C_m, \quad (1)$$

where i_{LCC} is the current of a single LCC, i_{NCX} is the NCX current of a single CRU, N is the total number of CRUs in the cell, and m is the total number of LCCs in a CRU. Because the $I_{Ca,L}$ window current is extremely important in the genesis of EADs (17–21), we reformulated the Markov LCC model to allow the window current to be directly manipulated. This was necessary because the Markov LCC formulation in the AP model by Restrepo et al. (14) has many linked states, and it is not straightforward to alter the window current without affecting other properties of the current. Therefore, we adopted a Hodgkin-Huxley type of formulation modified from the model of Luo and Rudy (22), in which the window current can be directly altered by shifting the steady-state activation and inactivation curves. In addition, the Hodgkin-Huxley-type model can be directly modified based on whole-cell measurements of the channel kinetics. A full description of the computer model and the numerical methods used are presented in the Supporting Materials and Methods.

Myocyte experiments

Patch-clamp recordings and optical imaging of Ca in isolated mouse ventricular myocytes were carried out. Details of the experimental methods are described in the Supporting Materials and Methods. All procedures comply with UCLA Animal Research Committee policies.

RESULTS

EAD and DAD generation in the computer model

A straightforward method of inducing EADs in the model was to shift the voltage activation curve of $I_{Ca,L}$ to more negative voltages to increase the $I_{Ca,L}$ window current (17), mimicking the effects of Ca channel mutations that cause long QT syndrome, such as Timothy syndrome (23) and other disease conditions such as hypertrophy (18). This shift had very small effects on $I_{Ca,L}$ and the Ca transient under AP clamp conditions (Fig. S4 in the Supporting Material). Under free-running conditions in which the AP was not clamped, however, this small shift in the activation curve lengthened APD and resulted in EADs, which then had much larger effects on $I_{Ca,L}$ and the Ca transient. Conversely, a straightforward method of inducing DADs in the model was to raise $[Na]_i$, such as might occur in chronic heart failure (24); this increased intracellular Ca loading via NCX sufficiently to cause spontaneous SR Ca release during diastole. Elevating $[Na]_i$ increased the Ca transient that augmented Ca-dependent currents, such as I_{NCX} and I_{Ks}, but also increased outward I_{NaK} (Fig. S4).

To study the interactions between EADs and DADs, we varied both parameters simultaneously. Fig. 1 summarizes the spectrum of AP behaviors observed for different hyperpolarizing left-shifts in the $I_{Ca,L}$ activation curve (0–9 mV) coupled with different levels of $[Na]_i$ (5–15 mM) during pacing at PCL = 2, 1, and 0.5 s, respectively. Six typical AP behaviors were observed at all PCLs, illustrated in the sample traces shown in Fig. 1 *D*: 1) normal AP, 2) EADs only, 3) repolarization failure, 4) DADs only, 5) a mixture of EADs and DADs, and 6) repolarization failure with voltage oscillations. More complex EAD and DAD behaviors, including TA, also occurred under specific conditions, which are discussed in detail later. In general, Fig. 1, *A–C*, shows that shifting the $I_{Ca,L}$ activation curve to more negative voltages promoted EADs and repolarization failure without inducing DADs. On the other hand, increasing $[Na]_i$ caused DADs by elevating $[Ca]_i$ and enhancing spontaneous SR Ca waves, but tended to suppress EADs and repolarization failure by increasing outward I_{NaK} and reducing inward (forward mode) NCX current. When both

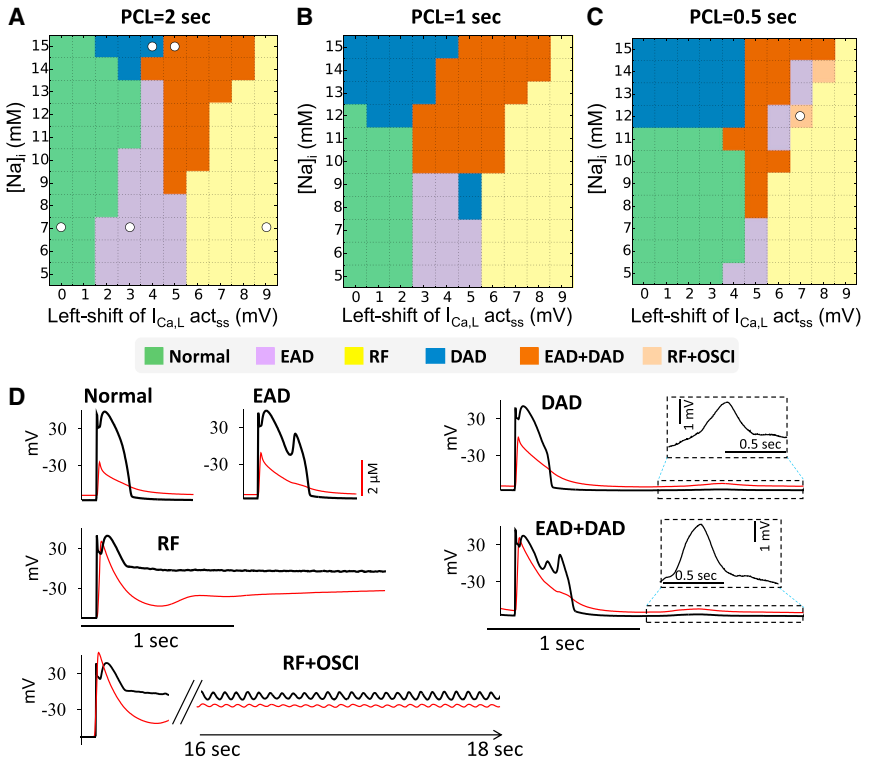

FIGURE 1 AP behaviors induced by shift in $I_{Ca,L}$ steady-state activation curve and $[Na]_i$. (*A–C*) Phase diagrams showing different AP behaviors by changing $[Na]_i$ and left-shifting the steady-state activation curve of $I_{Ca,L}$ at PCL = 2 s (*A*), 1 s (*B*), and 0.5 s (*C*). (*D*) Example traces of voltage and Ca for different AP behaviors taken from the parameter settings marked in (*A*) (*RF+OSCI* was from *C*). *RF*, repolarization failure without oscillations; *RF+OSCI*, repolarization failure with oscillations. To induce EADs, the open probability of the LCCs was increased by increasing $\alpha_{d'}$ from 0.3 to 1.5 ms^{-1} from the normal control case. Except for repolarization failure, we used 20 pacing beats for each parameter set to determine the AP behaviors. To see this figure in color, go online.

$I_{Ca,L}$ activation was shifted and $[Na]_i$ was elevated, EADs and DADs commonly occurred together.

The size of the regions exhibiting DADs or EADs varied with PCL. A faster heart rate (PCL = 0.5 s) expanded the DAD region, induced TA, and shrank the EAD region, whereas a slower heart rate (PCL = 2 s) had the converse effects. The results are consistent with experimental observations that EADs are often promoted by bradycardia, which reduces repolarization reserve, whereas DADs and TAs are often promoted by tachycardia, which exacerbates intracellular Ca loading. The combined EAD+DAD region was largest at the intermediate heart rate (PCL = 1 s). PCL had only minor effects on the normal AP and AP repolarization failure regions.

Modulation of EAD dynamics by Ca cycling

As shown in Fig. 1, *A–C*, when $I_{Ca,L}$ activation was left-shifted to induce EADs, elevating $[Na]_i$ promoted DADs but tended to suppress EADs, so that EADs were either replaced by DADs, or coexisted with DADs as $[Na]_i$ increased. The suppression of EADs occurred because elevating $[Na]_i$ enhanced outward I_{NaK} and inhibited inward I_{NCX}.

Because altered sarco/endoplasmic reticulum Ca ATPase (SERCA) activity and RyR leakiness are important features that impact Ca cycling in CPVT and heart failure, we also investigated the effects of these factors on EADs. At PCL = 2 s, doubling SERCA activity strongly promoted DADs but had only small and mixed effects on EADs, as can be seen by comparing the DAD and EAD regions in Fig. 2, *A* and *B*. Increasing RyR leakiness also strongly promoted DADs with only a small effect on suppressing EADs (compare Fig. 2, *A* and *C*). Combining both alterations enhanced these effects (Fig. 2 *D*). In this case, the amplitude of DADs also greatly increased, which caused DAD-mediated TA in both the pure DAD and mixed EAD+DAD regions. Because the TA occurred at a shorter cycle length than the PCL (Fig. 3 *D*), this also contributed to the suppression of EADs.

To illustrate the mechanisms by which SERCA activity and RyR leakiness affected EADs, representative AP and Ca-dependent ionic current traces are presented in Fig. 3. In Fig. 3 *A*, with $[Na]_i = 8$ mM, increasing SERCA activity promoted EADs. The peak of the Ca transient increased due to the greater SR Ca content, but the decay was accelerated due to more rapid SR Ca reuptake. These changes in the Ca transient caused: 1) a reduced peak $I_{Ca,L}$ due to stronger Ca-dependent inactivation, but almost no difference during the plateau phase until the EAD occurred; 2) a small decrease in I_{Ks} in the late plateau phase due to the lower $[Ca]_i$ (note that the K_d for Ca-dependent activation of I_{Ks} was set at 0.5 μM); and 3) increased I_{NCX} in the early phase but reduced I_{NCX} in the later phase of the plateau. The voltages were almost identical in the two cases until just before the EAD occurred, but the reduction in I_{Ks} predominated over the reduction in I_{NCX} to promote the EAD. The converse outcome is illustrated in Fig. 3 *B* when $[Na]_i$ was raised to

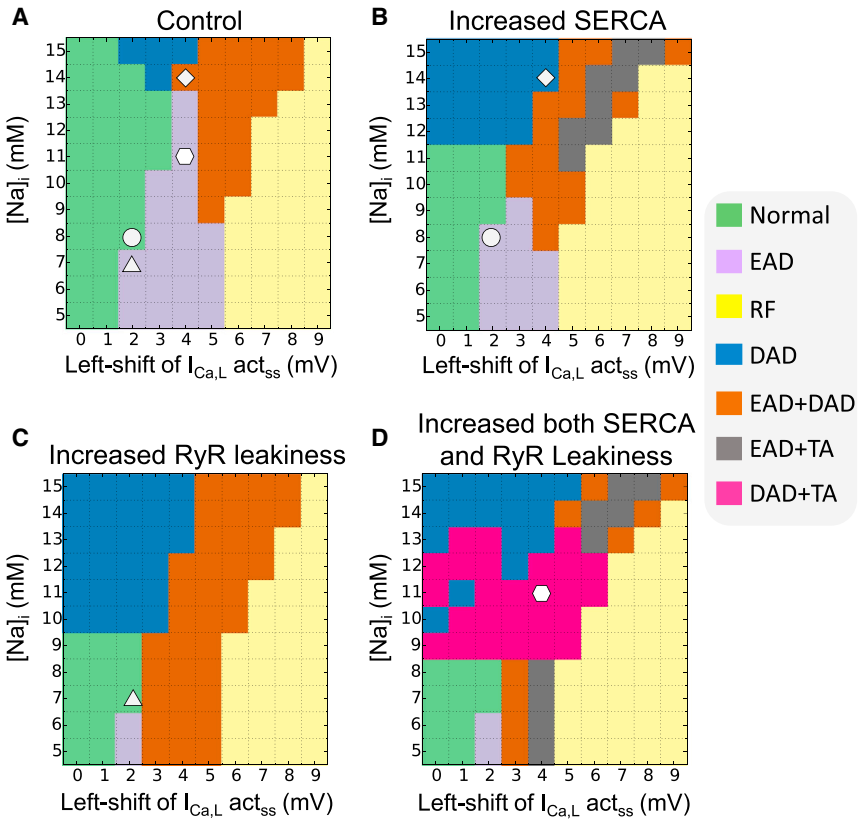

FIGURE 2 Phase diagrams showing modulation of EAD-DAD dynamics by Ca cycling properties at PCL 2 s. (*A*) Control (same as Fig. 1 *A*). (*B*) SERCA activity doubled. (*C*) RyR leakiness was increased by setting the transition rate from close to open to be threefold of the control value. (*D*) Combined increased SERCA activity and RyR leakiness. (*Marked symbols* are the parameter sets for the traces shown in Fig. 3.) To see this figure in color, go online.

14 mM. In this case, increasing SERCA did not increase the peak of the Ca transient, but still sped up its decay. This change had almost no effect on $I_{Ca,L}$ but reduced both I_{Ks} and I_{NCX}. In this case, reduction in I_{NCX} predominated over the reduction of I_{Ks}, and the EAD was suppressed. Fig. 3 *C* illustrates an example in which increasing RyR leakiness suppressed EADs. In this case, the Ca transient was smaller, which had a small effect on peak $I_{Ca,L}$ but reduced I_{Ks} and I_{NCX}. Similar to Fig. 3 *B*, the reduction of I_{NCX} predominated, suppressing the EAD. Finally, Fig. 3 *D* shows an example of the combined effects of increasing RyR leakiness and SERCA activity together. In this case, EADs were suppressed and sustained DAD-mediated TA occurred at cycle length < 0.5 s, shorter than the PCL of 2 s.

The results shown above demonstrate that the effects of Ca-voltage coupling are complex and nonintuitive, affecting multiple ionic currents in subtle ways to suppress or potentiate EADs and DADs. For example, in our model, increasing RyR leakiness suppressed EADs due to a smaller Ca transient. This finding generally agrees with previous experimental observations (25,26) that a larger Ca transient under Ca overload conditions tended to promote EADs via increased I_{NCX}. On the other hand, a recent study by Terentyev et al. (27) demonstrated that increased RyR leakiness caused a smaller Ca transient but nevertheless promoted EADs in long QT rabbit ventricular myocytes, illustrating the complexity of the interactions.

Spontaneous Ca oscillations and EADs

Spontaneous Ca oscillations associated with EADs have been observed in many experimental studies (10,11,13,28,29), and have been interpreted to be the cause of EADs when an intracellular Ca rise precedes the EAD upstroke (28). Supporting this conjecture, other experiments have shown that Ca oscillations associated with EADs can persist after voltage is clamped (13). However, the validity of these criteria for concluding that EADs can be caused by spontaneous Ca release events has not been quantitatively validated. In our computer simulations, we also observed these phenomena, as illustrated in Fig. 4 *A*. Following a long AP with multiple EADs, a subsequent DAD triggered a second AP (marked by an *asterisk*) with a single EAD (marked by *arrow*). Differing from other cases shown earlier (Figs. 1 and 3), the Ca transient during the EAD was much larger and started to rise (~10 ms) before voltage. In particular, the Ca concentration in dyadic space (DS) ($[Ca]_p$) rose much earlier than the EAD upstroke (*arrow* in Fig. 4 *B*). The line scan of $[Ca]_i$ was also dysynchronous, consistent with multiple spontaneous SR Ca release sites rather than a voltage-driven SR Ca release. These features agree with the above-mentioned experimental observations of spontaneous

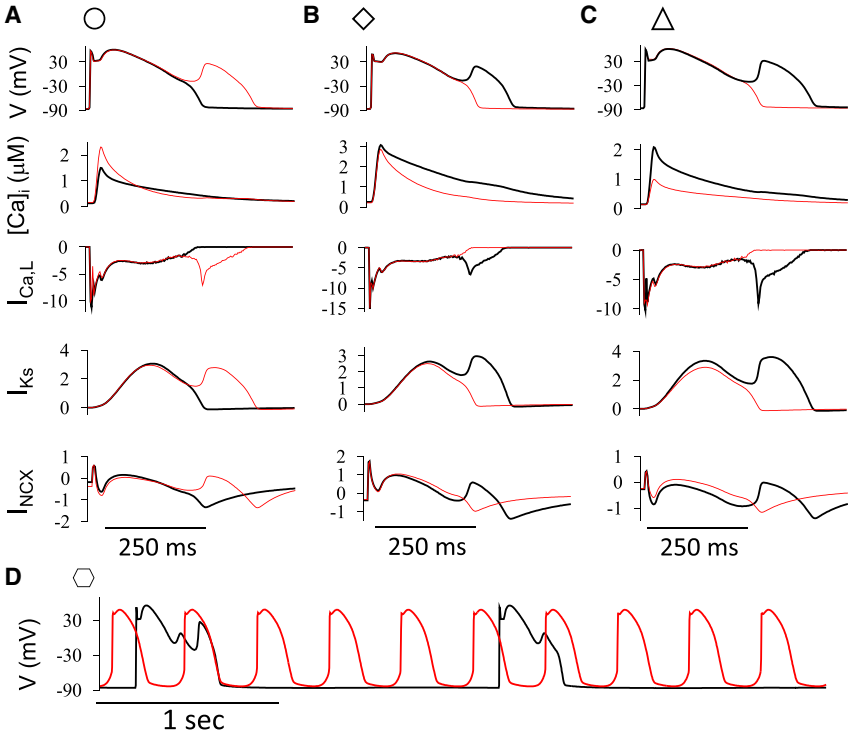

FIGURE 3 Comparison of APs and ionic currents before (*black traces*) and after (*red traces*) a change in Ca cycling. Indicating symbols for each case are parameter sets marked in Fig. 2. (*A*) Doubling SERCA activity with low $[Na]_i$ (8 mM) promoted EADs. (*B*) Doubled SERCA activity with high $[Na]_i$ (14 mM) suppressed EADs. (*C*) Increased RyR leakiness suppressed EADs. (*D*) Increased SERCA activity and RyR leakiness promoted DAD-driven TA and suppressed EADs. The unit of the currents is pA/pF. To see this figure in color, go online.

Ca release-induced EADs. To investigate the validity of this interpretation, we carried out additional simulations in which we either clamped voltage (Fig. 4 *B*) or clamped intracellular Ca (Fig. 4 *C*) at the EAD onset.

In the voltage-clamp case, voltage was clamped at the onset of the EAD period (marked by the *vertical dashed line* in Fig. 4 *B*) with a linear decay at different rates. When the voltage decay had a steeper slope (*red trace*), $[Ca]_i$ still rose during the clamped period as in the free-running case, although not as rapidly. This indicates that the initial $[Ca]_i$ rise was not triggered by the EAD, but was due to spontaneous (i.e., non-voltage-driven) Ca release. After the clamp was terminated, voltage repolarized to the resting potential, after which another spontaneous Ca release occurred several hundred milliseconds later, triggering a DAD-induced AP. In contrast, when the voltage decay had a shallower slope (*blue trace*), $[Ca]_i$ rose faster than in the steeper case, and after the voltage-clamp was released, both voltage and $[Ca]_i$ rose sharply due to reactivation of the LCCs (Fig. 4 *D*). Moreover, instead of repolarizing back to the resting potential, the voltage remained at the plateau level due to continuous opening of LCCs. Multiple EADs occurred with a frequency very different from that of the spontaneous Ca release. This is because after the first large release, most CRUs were refractory and could not respond to the first several EADs. Additional simulations at intermediate voltage decay slopes (not shown) defined a critical voltage at the end of the clamped period, below which no reactivation of LCCs occurred, and the cell repolarized to the resting potential. Above this value, reactivation of LCCs occurred, resulting in EADs. These findings indicate that the upstroke of the EAD requires the reactivation of LCCs and cannot be supported solely by I_{NCX} or other nonregenerative Ca-sensitive currents.

The consequences of clamping intracellular Ca, instead of voltage, during the EAD period are shown in Fig. 4 *C*. Because Ca concentrations varied at different locations in the cell, we clamped the Ca concentration in the DS at their existing values in all 19,305 CRUs, starting at the time when the mean Ca in the DS started to rise (marked by the *vertical dashed line* in Fig. 4 *C*). We then let Ca in the DS decay linearly at either a fast (*blue traces*) or slow (*red traces*) rate. In both cases, despite Ca in the DS being clamped, the voltage remained in the plateau range and oscillated with decrementing amplitude, eventually culminating in repolarization failure. It is interested to note that a faster Ca decay (*blue trace*) resulted in smaller EADs and a more stable plateau voltage. This is because when the clamp ended at a lower intracellular Ca, I_{NCX} was smaller but $I_{Ca,L}$ became larger (see Fig. 4 *D*) due to less Ca-depended inactivation. This increased window $I_{Ca,L}$, resulting in EADs and repolarization failure after intracellular Ca was clamped. The converse effect occurred in the free-running case, in which the progressive rise in Ca in the DS caused more $I_{Ca,L}$ inactivation, which suppressed the window $I_{Ca,L}$. This resulted in a lower take-off voltage for the EAD, which allowed a stronger voltage-dependent activation of LCCs to give rise to a larger depolarization. From this observation, we conclude although the amplitude of the EAD in the free-running case was potentiated by the increase in Ca preceding the

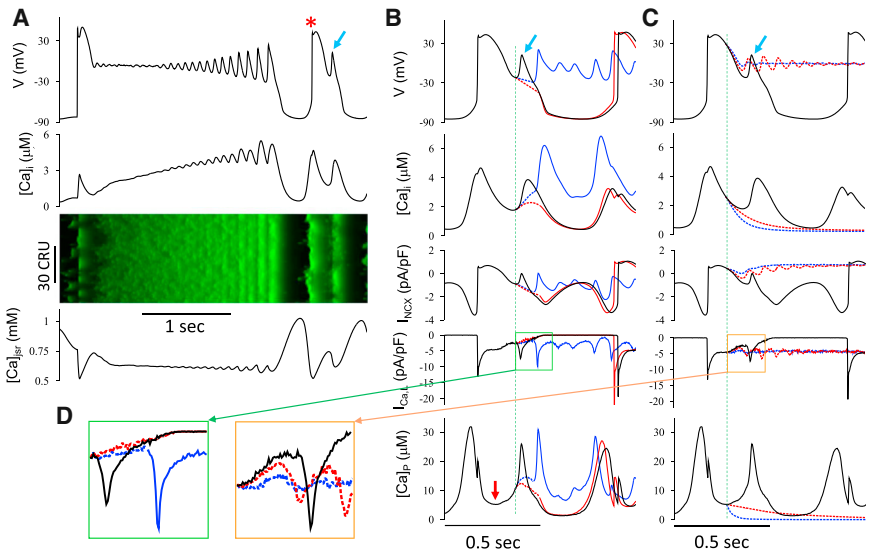

FIGURE 4 EADs elicited by spontaneous Ca release. (*A*) Voltage, $[Ca]_i$, $[Ca]_{jSR}$ versus time, and line scan of $[Ca]_i$ showing an EAD elicited by spontaneous Ca release (*arrow*) after an AP with multiple EADs. (*Asterisk*) AP triggered by a DAD. (*B*) Voltage, $[Ca]_i$, I_{NCX}, $I_{Ca,L}$, and Ca concentration in DS ($[Ca]_p$) versus time from the second AP in (*A*) (*black trace*). (*Superimposed red* and *blue traces*) Effects of voltage-clamping the model with a steeply (*red*) or slowly (*blue*) repolarizing voltage-clamp at the onset of the EAD (*vertical dashed line*). (*Arrow* in the $[Ca]_p$ trace) Time of spontaneous rise of Ca, which occurred much earlier than the onset of the EAD. (*C*) Same as (*B*), but $[Ca]_p$ was clamped with a slow (*red*) and a fast (*blue*) decay, and the clamp began when spontaneous $[Ca]_p$ rise started (*vertical dashed line*). (*D*) Enlarged views of $I_{Ca,L}$ from the clamping period (see *boxes* in *B*, *left panel*, and *C*, *right panel*). The parameters are the same as in Fig. 2 *B* (SERCA activity doubled, $[Na]_i$ = 15 mM and 7 mV left-shift in act_{ss} of $I_{Ca,L}$). Note: for Ca concentrations in this study, the line graphs are for whole-cell concentrations averaged over space while line scans show local concentrations in space. To see this figure in color, go online.

EAD upstroke, the EAD was driven primarily by the LCC reactivation-mediated voltage oscillation, and not underlying Ca oscillations.

These voltage- and Ca-clamp simulations demonstrate the following important mechanistic points. 1) A spontaneous Ca release event preceding the upstroke of an EAD does not necessarily imply that the spontaneous Ca release event is the cause of the EAD; rather, it participates, together with LCC reactivation, in the initiation of the EAD upstroke. 2) The role of spontaneous Ca release is complex—it can suppress EAD amplitude by facilitating Ca-dependent inactivation of LCCs, or enhance EAD amplitude for the same reason depending on the voltage range and balance of other contributing factors.

Modulation of DAD dynamics by voltage

To study the effects of voltage on DADs, we first studied conditions producing a small DAD shown in Fig. 5 *A*. In an experimental study in canine hearts by Burashnikov and Antzelevitch (30), blocking I_{Ks} prolonged APD, which increased Ca loading sufficiently to induce DADs. Here, we also reduced I_{Ks} to study how APD affects DADs. As I_{Ks} was gradually reduced, APD was prolonged and EADs were induced (Fig. 5 *B*). The additional Ca loading by the EAD caused the DAD to occur earlier with a larger amplitude (Fig. 5 *B*). Fig. 5, *C–F*, plots DAD amplitude versus APD (*C*), DAD coupling interval versus APD (*D*), DAD amplitude versus SR load (*E*), and DAD amplitude versus the diastolic $[Ca]_i$ preceding the DAD (*F*), respectively. The DAD amplitude increased almost linearly with APD in either the absence (*circles*) or the presence (*triangles*) of EADs. The DAD coupling interval deceased as APD increased. In the absence of EADs, the SR load increased with APD, which in turn increased DAD amplitude.

Note, however, that diastolic $[Ca]_i$ preceding the DAD did not increase significantly. In the presence of EADs, the SR load was near maximal and did not increase further as multiple EADs further prolonged APD. But despite the constant SR load, DAD amplitude continued to increase as APD was prolonged by EADs. The increase in DAD amplitude now tracked the progressive rise in diastolic $[Ca]_i$ preceding the DAD. As shown in the line scans (*insets*), in the case without EADs, Ca elevation was caused by random CRU firings, while in the case with EADs, Ca elevation was caused by more coordinated CRU firings (due to CRU recruitment). These results indicate: 1) regardless of whether EADs are present, lengthening APD increases Ca loading that promotes DADs and shortens the coupling interval; and 2) two mechanisms of DADs exist: the first depends only on the SR load, and the second depends on both the SR load and the diastolic $[Ca]_i$ level. Note that although APs with or without EADs were used to distinguish between the first and second behaviors in Fig. 5, EADs are not specifically required for the second DAD mechanism to occur. When EADs occur, however, the APD is much longer, enhancing Ca loading. Moreover, more LCCs open during EADs, which further enhances Ca load to potentiate the second mechanism.

Complex EAD dynamics in experiments

Some examples of complex EAD-DAD dynamics observed experimentally are illustrated in Fig. 6, obtained from

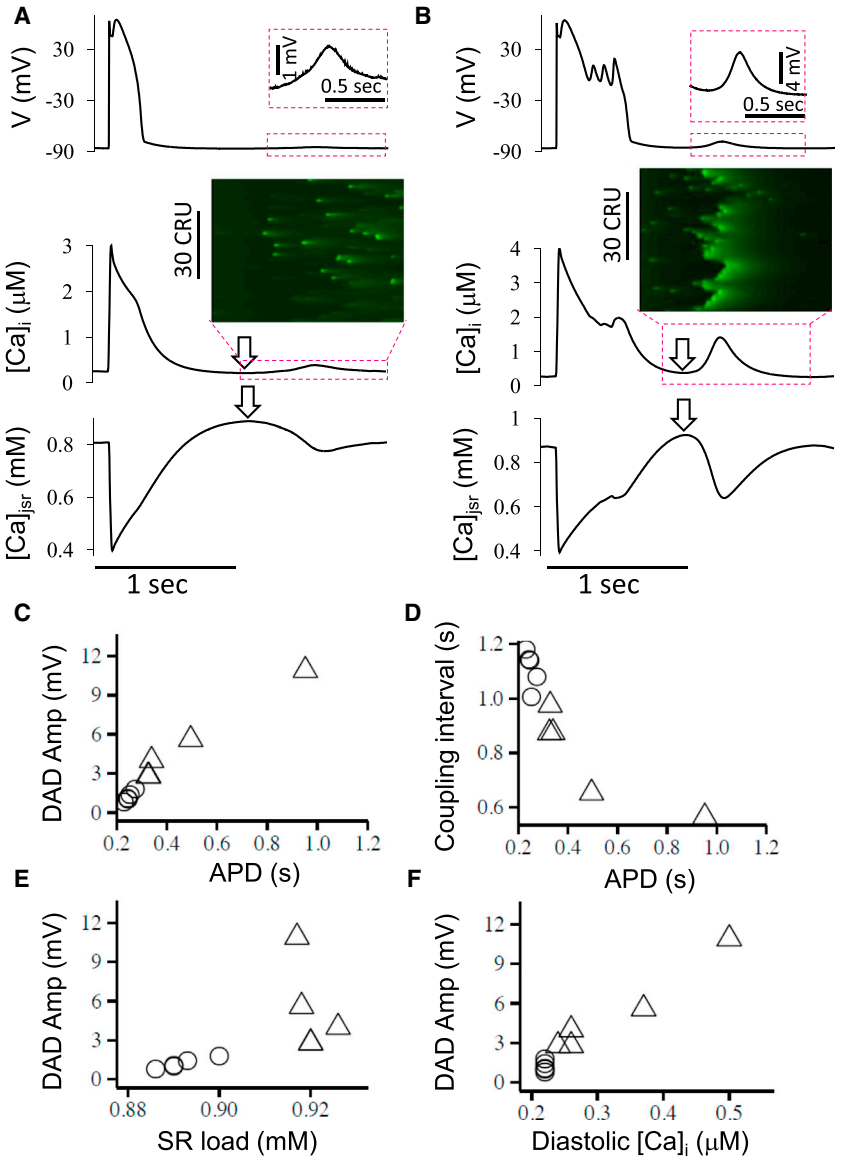

FIGURE 5 Modulation of DADs by APD. (*A*) Voltage, $[Ca]_i$, and $[Ca]_{jSR}$ versus time showing a regular AP followed by a small DAD. (*B*) Same as (*A*) but for a long AP with EADs followed by large DAD. (*Insets*) Line scans of $[Ca]_i$ during the DAD periods. (*C–F*) Plots of DAD amplitude versus APD (*C*), SR load (*E*), diastolic $[Ca]_i$ (*F*), and coupling interval versus APD (*D*) for DADs after APs of varying duration without (*circles*) or with (*triangles*) EADs. The definitions of SR load and diastolic $[Ca]_i$ (*arrows*) are indicated in (*A*) and (*B*). The coupling interval was defined as the interval from the end of the AP to the peak of the DAD. The parameters are the same as in Fig. 1 *A*, but under Ca overload ($[Ca]_o$ = 5 mM) with $[Na]_i$ = 10 mM and 1 mV left-shift in act_{ss} of $I_{Ca,L}$. The control I_{Ks} was used in (*B*) but was increased by a factor of 1.6 to shorten APD in (*A*). To see this figure in color, go online.

mouse ventricular myocytes loaded with Fluo-4-AM to record $[Ca]_i$ fluorescence. Myocytes were exposed to elevated $[Ca]_o$ (2.7 mM) to induce Ca overload. Fig. 6 *A* shows simultaneous membrane voltage, $[Ca]_i$ fluorescence, and a line scan of $[Ca]_i$ during an electrically stimulated AP in a patch-clamped myocyte (current clamp mode). Early in the plateau phase of the AP, both $[Ca]_i$ and voltage fluctuated with small amplitudes. Later, both $[Ca]_i$ and voltage began to oscillate with increasing amplitude until full repolarization occurred. The line scan of $[Ca]_i$ shows that Ca release exhibited random spatiotemporal dynamics in the early plateau phase, which then transitioned into synchronized oscillations in the late plateau phase.

Similar complex behaviors were observed in Fluo-4-AM loaded myocytes that were deliberately not patch-clamped so as to leave the intracellular milieu minimally perturbed. Fig. 6 *B* shows $[Ca]_i$ fluorescence and a line scan from such a myocyte, taken during a long recording in which all activity was spontaneous (see Fig. S6 for the entire recording). Although voltage was not directly recorded, AP upstrokes, DADs, EADs, and full repolarization can be generally inferred from the patterns of Ca release observed in the line scan, because voltage-gated Ca release is reflected by vertical lines and Ca waves by chevrons. In this tracing, a Ca wave in the upper portion of the line scan (*arrow*) initiated a triggered AP, in which multiple secondary Ca oscillations began immediately and grew in amplitude (reflecting EADs) before full repolarization. Repolarization was followed by two diastolic Ca waves (*chevrons*) that failed to trigger APs, after which a third Ca wave originating from the lower half of the line scan

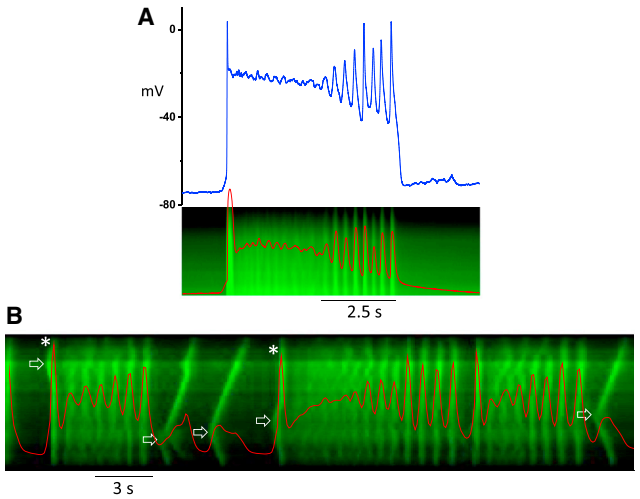

FIGURE 6 Complex EAD dynamics recorded from Fluo-4-AM-loaded mouse ventricular myocytes. (*A*) Voltage and $[Ca]_i$ fluorescence versus time, and line scan of $[Ca]_i$ measured from a patch-clamped mouse ventricular myocyte after a stimulus. (*B*) $[Ca]_i$ versus time, and line scan of $[Ca]_i$ recorded from a different isolated mouse ventricular myocyte that was not patch-clamped. No stimulus was given and the activity was spontaneous. (*Red traces* in the line scans) Integrated whole-cell Ca transients. (*Open arrows*) Initiation sites of the Ca waves that caused DADs or (*asterisk*) triggered APs. To see this figure in color, go online.

(*arrow*) triggered a second AP upstroke. Unlike the first AP, Ca oscillations during the second AP did not develop immediately, and the Ca release pattern was initially disordered, as evident from the line scan. The dysynchronous Ca release then gradually organized into synchronous oscillations with complex variations in amplitude. The largest release after the brief pause may reflect a late phase-3 EAD, because it did not appear to be triggered by a preceding Ca wave. After this event, the Ca oscillations became much smaller but quickly grew in amplitude, culminating in full repolarization, followed by a diastolic Ca wave (*chevron*) that failed to trigger an AP.

Several features are notable in both of these experimental recordings. When an AP was preceded by a relatively long diastolic interval (as in Fig. 6 *A* and the second AP in Fig. 6 *B*), the initial Ca transient during the AP upstroke was followed by dysynchronous Ca release with only small fluctuations in the plateau voltage and whole cell Ca. With time, however, these fluctuations self-organized into synchronous oscillations that subsequently grew progressively in amplitude, eventually culminating in full repolarization. In contrast, after a short diastolic interval (Fig. 6 *B*, first and third APs), the early phase of dysynchronous Ca releases did not occur, and synchronous Ca oscillations began immediately and grew rapidly, shortening the time to full repolarization. The features of the EADs generally agree with observations in previous experiments (e.g., long plateau, complex EAD pattern, and EAD-DAD interactions), as illustrated in Figs. S2 and S3.

Complex EAD dynamics in computer simulations

To analyze the mechanisms underlying complex EAD dynamics, we systematically scanned the parameters of the AP model with detailed Ca cycling to identify parameter regimes resembling the complex EAD (and DAD) dynamics, which were observed experimentally in the mouse myocytes in Fig. 6 and other species reported in the literature. Fig. 7 (also Fig. 4) illustrates a case similar to Fig. 6 *A*, in which the AP exhibited a very long plateau phase during which the voltage initially exhibited no or very small oscillations as the voltage slowly declined. This was followed by gradually increasing voltage oscillations generating progressively larger EADs culminating in full repolarization. This behavior has also been observed in many previously published experiments (examples are shown in Fig. S2) (31–37). In the model, $[Ca]_i$ increased gradually during the plateau phase with no significant Ca oscillations until after voltage oscillations developed. Both I_{NCX} and I_{Ks} slowly increased in concert with $[Ca]_i$. $I_{Ca,L}$ remained almost

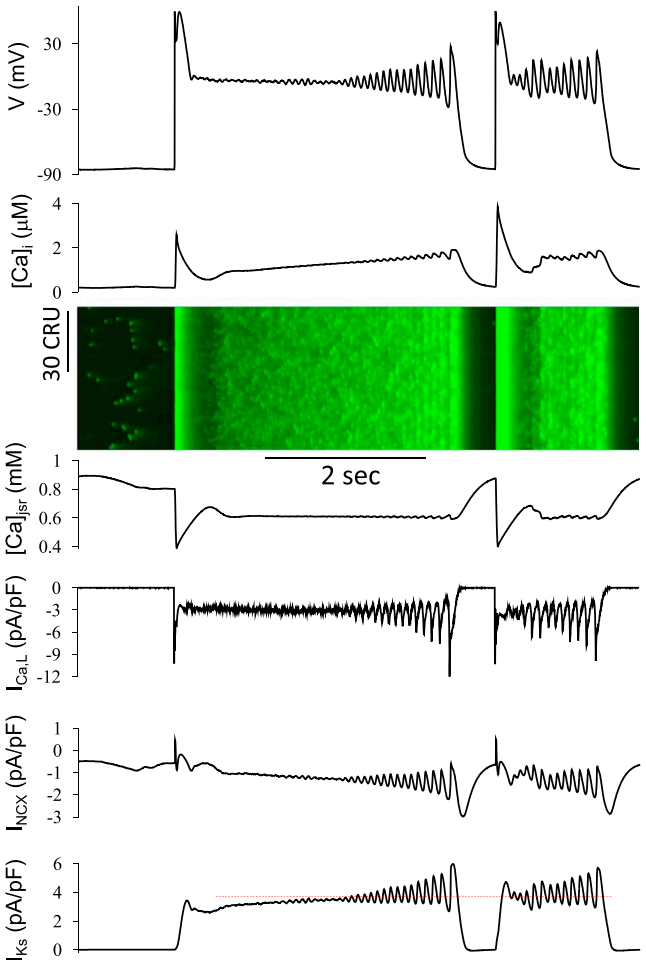

FIGURE 7 EAD onset after a long quasi-stable plateau phase. Shown are voltage, $[Ca]_i$, $[Ca]_{jSR}$, $I_{Ca,L}$, I_{NCX}, and I_{Ks} versus time, and a line scan of $[Ca]_i$. The parameters are the same as in Fig. 2 *A* with $[Na]_i = 7$ mM and a 5-mV left-shift in act_{ss} of $I_{Ca,L}$. To see this figure in color, go online.

constant until EADs occurred. The relatively stable SR Ca content indicates that the increase in $[Ca]_i$ resulted primarily from maintained Ca entry via $I_{Ca,L}$. As shown in the line scan, before the onset of frank EADs, Ca release exhibited a random spatiotemporal pattern—one that gradually became more synchronous as EADs developed. When the EADs reached a large enough amplitude, I_{Ks} activation became sufficient to induce full repolarization. A second paced AP was then elicited after a short diastolic interval. Similar to the second AP in Fig. 6 *B*, the long plateau disappeared and EADs and Ca oscillations began immediately as the voltage decayed into the LCC window voltage range.

Because the experiments in Fig. 6 were done in mouse ventricular myocytes exposed to elevated extracellular [Ca], we also carried out computer simulations using a mouse ventricular myocyte model with the ionic currents from the model by Morotti et al. (38) (see the Supporting Materials and Methods). Similar complex EAD behaviors and spontaneous APs were obtained (see Fig. S6), indicating that the behaviors are not model-specific.

EADs and Ca oscillations with alternating or more complex patterns are shown in Fig. 8. In this example, both the take-off potential and amplitude of the EADs exhibited a period-3-like pattern most of the time. Moreover, switching between EADs and DAD-mediated-triggered APs (*asterisks* in Fig. 8) occurred. These behaviors are similar to Fig. 6 as well as previous experiments (sample voltage traces are shown in Fig. S3) (3,31,37). Note that in Fig. 8, the first AP was elicited by a stimulus and the following three APs were triggered by DADs. As shown in Fig. 5, lengthening of APD by EADs causes excessive Ca loading of the cell, promoting spontaneous Ca release after full repolarization, resulting in DADs. Thus, the long APs with many EADs enhanced Ca overload and thus promoted DADs, illustrating a case of complex EAD and DAD interactions. The underlying mechanisms are addressed in the Discussion.

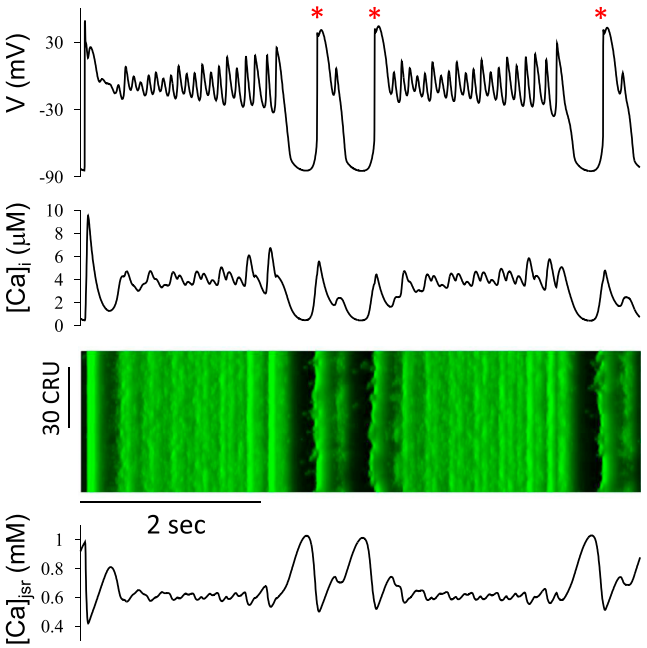

FIGURE 8 Complex EAD dynamics due to bidirectional voltage-Ca coupling. Voltage, $[Ca]_i$, and $[Ca]_{jSR}$ versus time, and a line scan of $[Ca]_i$. The parameters are the same as in Fig. 2 *B* (SERCA activity doubled with $[Na]_i = 14$ mM and a 7 mV left-shift in act_{ss} of $I_{Ca,L}$). (*Asterisks*) Spontaneous Ca-release-induced APs. To see this figure in color, go online.

DISCUSSION

EADs and DADs were first described more than a half century ago (39,40), and many EAD and DAD behaviors, from simple to very complex, have been observed in experiments. However, due to the complex interactions between voltage and Ca, it has been difficult to pinpoint experimentally the exact underlying mechanisms for different behaviors. Computer modeling and simulations are a complementary means to reveal the underlying ionic mechanisms. Many computer modeling studies (41–46) have been carried out to investigate the mechanisms of EADs, but for the most part these have focused on EADs caused by voltage-driven oscillations, because the AP models lacked detailed spatiotemporal Ca cycling required to simulate Ca waves and oscillations. In this study, we investigated the effects of bidirectional Ca-voltage coupling on the genesis of EADs and DADs in ventricular myocytes, using an AP model with a detailed spatiotemporal Ca cycling regulation incorporating stochastic LCC and RyR openings and experiments of mouse ventricular myocytes. Mechanistic insights we consider novel have been revealed, and these are discussed below.

Modulations of EADs by Ca cycling dynamics

It is well known that LCC window current is a key component for EADs (17–21), but all other currents during the plateau also contribute to the formation of the EADs (21,41). Using bifurcation analysis (21,44), we have previously identified the bifurcations that initiate and terminate the voltage oscillations, and characterized the contribution of each ionic current in generating these bifurcations. The Ca transient modulates EAD dynamics via its effects on multiple Ca-dependent ionic currents. Because the $[Ca]_i$ dependences of these inward and outward currents are different, the net effect of changing $[Ca]_i$ on the bifurcations and the time course of voltage oscillations is complex and often nonintuitive. Changing $[Ca]_i$ can either promote or suppress EADs, depending on the balance of factors under a given set of conditions (Figs. 2 and 3).

Spontaneous Ca oscillations have been proposed to cause EADs in a number of experimental studies (10,11,13,28,29), primarily based on evidence such as a rise in $[Ca]_i$ preceding the EAD upstroke (28), or continuation of spontaneous Ca oscillations when voltage oscillations were prevented by imposing an AP clamp (13). A fresh mechanistic insight

arising from our analysis is that the interpretation of these experimental findings may be overly simplistic. Intuitively, because voltage and Ca are coupled, if Ca oscillates in the repolarizing phase of the AP, voltage will also oscillate. However, based on our present simulations (Fig. 4), the role of spontaneous Ca oscillations as a pure mechanism for generating EADs is far from straightforward. First, I_{NCX} is not a regenerative current like $I_{Ca,L}$. That is, as voltage depolarizes during the EAD upstroke, I_{NCX} becomes weaker, not stronger. Because I_{NCX} is small and decreases as voltage rises, reactivation of $I_{Ca,L}$ is required for EADs to become large enough to generate TA and propagate in tissue. Thus, a spontaneous Ca release event can potentially initiate an EAD upstroke by activating I_{NCX}, but cannot generate significant EAD amplitude or TA without the participation of $I_{Ca,L}$ reactivation. This situation is further complicated by the interactions between intracellular Ca and $I_{Ca,L}$ inactivation, which inevitably affect the $I_{Ca,L}$ window current, the key driver for voltage-dependent EADs. As shown in Fig. 4, high intracellular Ca due to spontaneous Ca release just preceding the EAD strongly enhanced Ca-dependent inactivation of $I_{Ca,L}$, which offset its effect at increasing I_{NCX}. The consequence was a lower take-off potential of the EAD, which then resulted in a large-amplitude EAD due to greater $I_{Ca,L}$ reactivation. However, additional EADs were suppressed due to a stronger Ca-induced inactivation of $I_{Ca,L}$. This scenario may be relevant to isoproterenol-induced EADs, which typically exhibit only one EAD in each AP, with two or more EADs per AP being rare (10,11,13). In summary, the modeling results show that the effect of spontaneous Ca release events on EAD genesis is extremely complex, and intuitive interpretations, like assuming that the timing of the intracellular Ca rise relative to the EAD upstroke implies causality, are overly simplistic.

Mechanisms of DADs

It is widely accepted that DADs are mediated by Ca waves (47–50), in which spontaneous SR Ca release from a group of adjacent CRUs recruits neighboring CRUs to initiate a propagating wave (51,52). On the other hand, the simulations in Fig. 5 *A* demonstrate, to our knowledge, a novel mechanism of small DADs with long coupling intervals in the absence of Ca waves, purely by synchronous resetting of the recovery period of CRUs by an AP, without recruitment. In this case, after an AP with normal Ca release, the SR Ca rose to a level higher than its equilibrium load. This occurred because the SERCA pump is fast relative to NCX, causing the SR to refill to a higher level. After the CRUs had recovered from the preceding normal AP, spontaneous CRU firings occurred due to high SR Ca load, which summed to produce a small whole-cell $[Ca]_i$ increase eliciting a small DAD. As seen in the line scans in Fig. 5 *A*, the release events were random individual CRU firings that did not propagate to neighboring CRUs. In contrast, in Fig. 5 *B*, the EADs during the AP greatly enhanced the cellular Ca load, elevating diastolic $[Ca]_i$. In this case, when CRUs fired during the subsequent diastole, they propagated as mini-waves, facilitated by both the high SR Ca content and the elevated diastolic $[Ca]_i$ level. Therefore, in the non-Ca-wave-mediated mechanism of DADs in Fig. 5 *A*, the high SR Ca load due to fast SERCA pump activity after an AP synchronizes the subsequent diastolic spontaneous Ca release by independently firing CRUs. However, diastolic $[Ca]_i$ is not sufficiently elevated for these Ca sparks to trigger propagating Ca waves. For this reason, only a single DAD occurs after the AP. On the other hand, in the Ca-wave-mediated mechanism, diastolic $[Ca]_i$ as well as SR Ca load both become important by facilitating CRU recruitment to form Ca waves, and multiple DADs can be seen after an AP. Finally, although not addressed in this study, DAD amplitude is determined not only by the synchronicity of spontaneous Ca release, but also by the Ca-voltage coupling gain (53,54), i.e., the amplitude of the Ca-sensitive currents such as I_{NCX} and $I_{ns(Ca)}$ activated by the spontaneous Ca transient in relation to the outward currents opposing depolarization, principally I_{K1} in ventricular tissue.

Mechanisms of complex EAD patterns

As shown in Figs. 6, 7, 8, and S1–S3, EADs can exhibit very complex patterns and behaviors. From this study and the nonlinear dynamics analysis (21,44), we can provide a unified theory for these complex EAD patterns based on the interactions of Ca dynamics with the Hopf-homoclinic bifurcation mechanism of voltage-driven EADs. Fig. 9 shows a schematic diagram illustrating the bifurcations leading to and terminating EADs. By 100–200 ms after the AP upstroke, most currents have reached quasi-steady states except for slow currents, including slowly activating I_{Ks}, slowly inactivating late I_{Na}, slow accumulation of

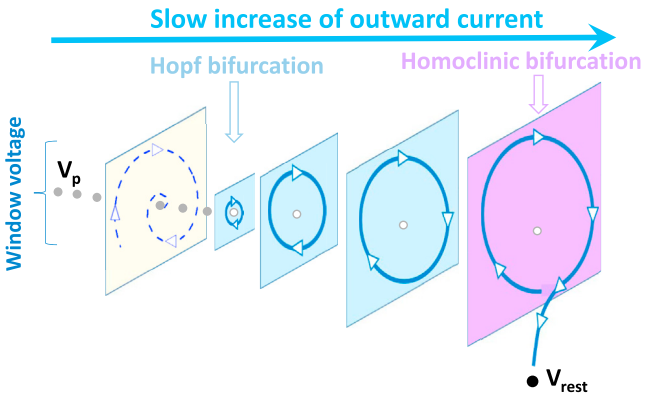

FIGURE 9 Schematic diagrams for the mechanisms of EADs. Schematic diagram showing the bifurcations for EADs. The value V_p is the quasi-equilibrium steady-state voltage in the plateau, and V_{rest} is the resting potential. To see this figure in color, go online.

$[Na]_i$ causing slowly changing I_{NaK}, etc. The inward currents and the outward currents are roughly equal during the AP plateau, forming a quasi-equilibrium state. As time continues, slowly increasing outward currents progressively activate, destabilizing the quasi-equilibrium state and initiating oscillations via a Hopf bifurcation. As the net outward current at the trough of the EADs becomes progressively larger during the voltage oscillations, the system approaches another bifurcation point, called a homoclinic bifurcation, at which the oscillation terminates because the inward current is no longer strong enough to prevent the voltage from repolarizing, leading to full repolarization in the resting potential. Depending on the stability of the quasi-equilibrium state, the decay rate of voltage, and the activation speed of the slowly increasing net outward current, as well as Ca-voltage coupling, different EAD patterns can occur. Based on the bifurcation theory and results in previous simulations (21,44,55–57) and the observations in this study, we summarize below the mechanisms underlying six characteristic patterns of EAD behaviors:

EADs with growing amplitude

This is the most widely seen EAD pattern in experiments (Fig. S1 *A*) and computer simulations. As shown in Fig. 9, after the Hopf bifurcation point, the oscillation amplitude grows as the slowly increasing outward current makes the trough of the EAD more and more negative, reaching a maximum at the homoclinic bifurcation point. If voltage decays into the window voltage range at roughly the same time as the slowly increasing outward current increases to the level sufficient to initiate the Hopf bifurcation, then the EAD amplitude will grow from very small oscillations to the maximum oscillation at the homoclinic bifurcation point before full repolarization.

EADs with decreasing amplitude (Fig. S1 B)

Although the quasi-equilibrium state is stable before the Hopf bifurcation point, the voltage entering into the window range may spiral toward the quasi-equilibrium (see the *spiral curve* in Fig. 9), resulting in a transiently decreasing oscillation amplitude. If the Hopf-homoclinic bifurcation does not exist, then the oscillation gradually dampens out until repolarization to the resting potential occurs, resulting in EADs with decreasing amplitude. This scenario was analyzed in detail using bifurcation theory by Xie et al. (56).

EADs with decreasing and then increasing amplitude (Fig. S2 A)

If voltage decays into the window range earlier than the Hopf bifurcation, then the voltage may oscillate transiently with decreasing amplitude (see the *spiral curve* in Fig. 9). As the slowly increasing outward current increases to the critical value initiating the Hopf bifurcation, oscillation resumes with a growing amplitude, reaching its maximum at the homoclinic bifurcation point.

EADs after a long plateau (Figs. 6, 7, and S2, A and B)

If voltage decays to the plateau level much earlier than the Hopf bifurcation, it will remain at the plateau voltage until the slow outward current increases sufficiently to induce the Hopf bifurcation for oscillations. Therefore, the duration of the plateau depends on the speed of the slowly growing outward current (or slowly decreasing inward current). In the simulation in Fig. 7 using our AP model based on rabbit ventricle, I_{Ks} is the slowly increasing current, such that the onset of oscillations is very sensitive to I_{Ks} (Fig. 7): the plateau is shorter when I_{Ks} starts at a larger value (referenced by the *dashed horizontal line* in the I_{Ks} trace in Fig. 7), e.g., after a short diastolic interval.

A key question is why the intracellular Ca, despite being quite high, does not oscillate during the long plateau phase until EADs are present. To reveal the underlying mechanisms, we did a series of simulations under different voltage-clamp conditions (see Figs. S7 and S8 and description). We showed that random LCC openings trigger spatiotemporally random CRU firings, which prevent the CRUs from recovering synchronously as required for spontaneous Ca oscillations. After the Hopf bifurcation, however, the voltage oscillations cause LCC openings to synchronize, which synchronizes the CRU openings, so that voltage and Ca oscillate together.

Although I_{Ks} played the major role as the slowly increasing outward current in our AP model based on rabbit ventricle, other slowly changing currents can also play the equivalent role, and may be more important in other species. For example, $[Na]_i$ accumulates very slowly, causing a very slow increase in I_{NaK}, which can also initiate the Hopf-homoclinic bifurcation, as shown in our previous simulations (57). Late I_{Na} is another candidate because it may slowly inactivate (58). Finally, the gradual rise in $[Ca]_i$ may also activate other outward currents, such as the Ca-activated Cl current ($I_{Cl(Ca)}$) (59) or small conductance Ca-activated K current (60). Because I_{Ks} has a very low density in mouse ventricular myocytes, one or more of these currents may be responsible for the slow process that is causing the long plateau shown in the experimental recordings in Fig. 6.

EAD bursts (Fig. S2 C)

If voltage quickly decays into window voltage for oscillations and then outward current increases very slowly through the Hopf-homoclinic bifurcation window, a very long EAD burst can result. As demonstrated in our previous simulations (57), the slow accumulation of $[Na]_i$ causing a very slow increase of I_{NaK} can be a candidate for finally terminating the long-lasting EAD burst.

EAD alternans and more complex EAD patterns (Figs. 6, 8, and S3)

To our knowledge, a key novel finding of this study is that the Hopf-Homoclinic bifurcation dynamics alone do not explain

alternating and more complex EAD patterns. As shown by the simulations in Figs. S7 and S8, EAD alternans arises as a result of Ca-voltage coupling when voltage oscillations during EADs encounter CRU refractoriness, generating Ca transient alternans or more complex patterns. The Ca transient behaviors then feed-back to affect the amplitude of the EADs via Ca-sensitive currents, or via frequency competition of voltage oscillation and spontaneous Ca oscillations. Therefore, EAD alternans and more complex EAD patterns directly result from bidirectional Ca-voltage coupling.

Limitations

Several limitations should be noted. The AP and spatiotemporal Ca cycling model in this study simulates a three-dimensional network of CRUs representing a ventricular myocyte, but it is still much simpler than a real myocyte (61,62). Heterogeneous ion channel densities and CRU properties may potentially introduce novel dynamics not captured in a homogeneous model. However, the homogeneous model appears to capture most of the experimentally observed behaviors, and in addition provides a key framework for future exploration of the role of heterogeneity. The RyR model developed by Restrepo et al. (14) incorporated calsequestrin-mediated SR luminal Ca regulation, whereas recent experiments have demonstrated a luminal Ca-sensing site in the RyR mediating this effect (63). Moreover, the refractoriness of Ca release is controversial, with a wide range of experimentally measured values (64–69) and different proposed causes. Different refractory period choices may impact the Ca cycling dynamics, as well as the voltage dynamics caused by Ca-voltage coupling. In our model, the effects of Ca on EADs are mediated through direct effects on ionic currents. It is well known that Ca-dependent signaling pathways, such as CaMKII signaling, can affect many ionic currents as well as Ca cycling properties (70), which can have much more complex effects on EADs and DADs. Our AP model does not include some of the Ca-dependent ionic currents, such as $I_{ns(Ca)}$ (71,72) and the small conductance Ca-activated K channel (60), which may play important roles in bidirectional Ca-voltage coupling and Ca-dependent EAD genesis. In addition, we have clamped $[Na]_i$ in this study. It has been shown that elevation of $[Ca]_i$ causing activation of CaMKII enhances late I_{Na}, which further elevates $[Na]_i$, causing further elevation of $[Ca]_i$ (38). Therefore, a dynamic $[Na]_i$ may have additional effects on EADs and DADs.

Another limitation is that the specific ionic mechanisms of EADs may vary among different species. For example, in the rabbit model, slow activation of I_{Ks} plays a key role in the EAD dynamics, whereas I_{Ks} is a very small current in mouse ventricular myocytes. As discussed earlier, however, I_{Ks} is not the only slow component that can play this role in the dynamics. Other candidates include slow Na accumulation activating outward I_{NaK}, the progressive Ca accumulation activating $I_{Cl(Ca)}$, and/or slow inactivation of late I_{Na}, all of which can in principle replace the role of I_{Ks} in initiating and terminating EADs via the Hopf-homoclinic bifurcation scenario. In the mouse ventricular cell model in which I_{Ks} is insignificant, the slow inactivation of late I_{Na} substitutes for the role of I_{Ks} in the rabbit ventricular cell model (see Supporting Materials and Methods and Fig. S6). Because the complex EAD behaviors have been widely observed in many different types of cardiac cells and species exposed to varying pathophysiological stresses (e.g., Figs. 6 and S1–S3), we believe that different species and cell types share a common general dynamical mechanism, i.e., the Hopf-homoclinic bifurcation scenario depicted in Fig. 9. Our study focused mainly on phase-2 EADs and DADs, and did not address phase-3 EADs, which may involve additional or different mechanisms.

Finally, although our simulation results of complex EAD behaviors agree well with our own experimental observations and those from the literature, some of the theoretical predictions of our study need to be validated by future experiments. These would include the complex effects of the amplitude and morphology of Ca transient on modulating EADs, the effects of spontaneous Ca release on generating and suppressing EADs, and the non-Ca-wave-mediated DADs.

SUPPORTING MATERIAL

Supporting Materials and Methods, nine figures, and ten tables are available at http://www.biophysj.org/biophysj/supplemental/S0006-3495(15)00244-1.

AUTHOR CONTRIBUTIONS

Z.Q. designed the overall research and supervised the simulations; Z.S. contributed to the overall research design and performed the simulations; J.N.W. contributed to the overall research design and supervised the biological experiments; C.Y.K. contributed to the overall research design and performed the biological experiments; M.N. contributed to the overall design; Z.S., C.Y.K., J.N.W., and Z.Q. analyzed data; and Z.S., C.Y.K., J.N.W., and Z.Q. wrote the article.

ACKNOWLEDGMENTS

This work is supported by National Institutes of Health grants No. P01 HL078931, No. R01 HL110791, and No. R56 HL118041, a research grant from Gilead Sciences (to Z.S.), and Laubisch and Kawata endowments.

REFERENCES

1. Keating, M. T., and M. C. Sanguinetti. 2001. Molecular and cellular mechanisms of cardiac arrhythmias. *Cell.* 104:569–580.
2. Clancy, C. E., M. Tateyama, and R. S. Kass. 2002. Insights into the molecular mechanisms of bradycardia-triggered arrhythmias in long QT-3 syndrome. *J. Clin. Invest.* 110:1251–1262.
3. Liu, G. X., B. R. Choi, …, G. Koren. 2012. Differential conditions for early after-depolarizations and triggered activity in cardiomyocytes

derived from transgenic LQT1 and LQT2 rabbits. *J. Physiol.* 590:1171–1180.

4. Györke, S. 2009. Molecular basis of catecholaminergic polymorphic ventricular tachycardia. *Heart Rhythm.* 6:123–129.
5. Mohamed, U., C. Napolitano, and S. G. Priori. 2007. Molecular and electrophysiological bases of catecholaminergic polymorphic ventricular tachycardia. *J. Cardiovasc. Electrophysiol.* 18:791–797.
6. Li, G. R., C. P. Lau, …, S. Nattel. 2002. Transmural action potential and ionic current remodeling in ventricles of failing canine hearts. *Am. J. Physiol. Heart Circ. Physiol.* 283:H1031–H1041.
7. Yeh, Y. H., R. Wakili, …, S. Nattel. 2008. Calcium-handling abnormalities underlying atrial arrhythmogenesis and contractile dysfunction in dogs with congestive heart failure. *Circ. Arrhythm. Electrophysiol.* 1:93–102.
8. Rosen, M. R., A. L. Wit, and B. F. Hoffman. 1975. Electrophysiology and pharmacology of cardiac arrhythmias. IV. Cardiac antiarrhythmic and toxic effects of digitalis. *Am. Heart J.* 89:391–399.
9. Qu, Z., G. Hu, …, J. N. Weiss. 2014. Nonlinear and stochastic dynamics in the heart. *Phys. Rep.* 543:61–162.
10. Priori, S. G., and P. B. Corr. 1990. Mechanisms underlying early and delayed afterdepolarizations induced by catecholamines. *Am. J. Physiol.* 258:H1796–H1805.
11. Volders, P. G., A. Kulcśar, …, B. Szabo. 1997. Similarities between early and delayed afterdepolarizations induced by isoproterenol in canine ventricular myocytes. *Cardiovasc. Res.* 34:348–359.
12. Volders, P. G., M. A. Vos, …, R. Lazzara. 2000. Progress in the understanding of cardiac early afterdepolarizations and torsades de pointes: time to revise current concepts. *Cardiovasc. Res.* 46:376–392.
13. Zhao, Z., H. Wen, …, L. H. Xie. 2012. Revisiting the ionic mechanisms of early afterdepolarizations in cardiomyocytes: predominant by Ca waves or Ca currents? *Am. J. Physiol. Heart Circ. Physiol.* 302:H1636–H1644.
14. Restrepo, J. G., J. N. Weiss, and A. Karma. 2008. Calsequestrin-mediated mechanism for cellular calcium transient alternans. *Biophys. J.* 95:3767–3789.
15. Chen, W., J. A. Wasserstrom, and Y. Shiferaw. 2009. Role of coupled gating between cardiac ryanodine receptors in the genesis of triggered arrhythmias. *Am. J. Physiol. Heart Circ. Physiol.* 297:H171–H180.
16. Nivala, M., E. de Lange, …, Z. Qu. 2012. Computational modeling and numerical methods for spatiotemporal calcium cycling in ventricular myocytes. *Front. Physiol.* 3:114.
17. Madhvani, R. V., Y. Xie, …, R. Olcese. 2011. Shaping a new Ca^{2+} conductance to suppress early afterdepolarizations in cardiac myocytes. *J. Physiol.* 589:6081–6092.
18. Antoons, G., P. G. Volders, …, K. R. Sipido. 2007. Window Ca^{2+} current and its modulation by Ca^{2+} release in hypertrophied cardiac myocytes from dogs with chronic atrioventricular block. *J. Physiol.* 579:147–160.
19. January, C. T., and J. M. Riddle. 1989. Early afterdepolarizations: mechanism of induction and block. A role for L-type Ca^{2+} current. *Circ. Res.* 64:977–990.
20. January, C. T., V. Chau, and J. C. Makielski. 1991. Triggered activity in the heart: cellular mechanisms of early after-depolarizations. *Eur. Heart J.* 12 (*Suppl. F*):4–9.
21. Qu, Z., L.-H. Xie, …, J. N. Weiss. 2013. Early afterdepolarizations in cardiac myocytes: beyond reduced repolarization reserve. *Cardiovasc. Res.* 99:6–15.
22. Luo, C. H., and Y. Rudy. 1994. A dynamic model of the cardiac ventricular action potential. I. Simulations of ionic currents and concentration changes. *Circ. Res.* 74:1071–1096.
23. Hennessey, J. A., N. J. Boczek, …, G. S. Pitt. 2014. A CACNA1C variant associated with reduced voltage-dependent inactivation, increased $Ca_V1.2$ channel window current, and arrhythmogenesis. *PLoS ONE.* 9:e106982.
24. Despa, S., M. A. Islam, …, D. M. Bers. 2002. Intracellular Na^+ concentration is elevated in heart failure but Na/K pump function is unchanged. *Circulation.* 105:2543–2548.
25. Burashnikov, A., and C. Antzelevitch. 1998. Acceleration-induced action potential prolongation and early afterdepolarizations. *J. Cardiovasc. Electrophysiol.* 9:934–948.
26. Szabo, B., T. Kovacs, and R. Lazzara. 1995. Role of calcium loading in early afterdepolarizations generated by Cs^+ in canine and guinea pig Purkinje fibers. *J. Cardiovasc. Electrophysiol.* 6:796–812.
27. Terentyev, D., C. M. Rees, …, G. Koren. 2014. Hyperphosphorylation of RyRs underlies triggered activity in transgenic rabbit model of LQT2 syndrome. *Circ. Res.* 115:919–928.
28. Choi, B. R., F. Burton, and G. Salama. 2002. Cytosolic Ca^{2+} triggers early afterdepolarizations and torsade de pointes in rabbit hearts with type 2 long QT syndrome. *J. Physiol.* 543:615–631.
29. Odening, K. E., B. R. Choi, and G. Koren. 2012. Sex hormones and cardiac arrest in long QT syndrome: does progesterone represent a potential new antiarrhythmic therapy? *Heart Rhythm.* 9:1150–1152.
30. Burashnikov, A., and C. Antzelevitch. 2000. Block of i_{Ks} does not induce early afterdepolarization activity but promotes β-adrenergic agonist-induced delayed afterdepolarization activity. *J. Cardiovasc. Electrophysiol.* 11:458–465.
31. Aronson, R. S. 1981. Afterpotentials and triggered activity in hypertrophied myocardium from rats with renal hypertension. *Circ. Res.* 48:720–727.
32. el-Sherif, N., R. H. Zeiler, …, R. Henkin. 1988. QTU prolongation and polymorphic ventricular tachyarrhythmias due to bradycardia-dependent early afterdepolarizations. Afterdepolarizations and ventricular arrhythmias. *Circ. Res.* 63:286–305.
33. Surawicz, B. 1989. Electrophysiologic substrate of torsade de pointes: dispersion of repolarization or early afterdepolarizations? *J. Am. Coll. Cardiol.* 14:172–184.
34. Adamantidis, M. M., P. Kerram, …, B. A. Dupuis. 1993. Droperidol exerts dual effects on repolarization and induces early afterdepolarizations and triggered activity in rabbit Purkinje fibers. *J. Pharmacol. Exp. Ther.* 266:884–893.
35. Puisieux, F. L., M. M. Adamantidis, …, B. A. Dupuis. 1996. Cisapride-induced prolongation of cardiac action potential and early afterdepolarizations in rabbit Purkinje fibers. *Br. J. Pharmacol.* 117:1377–1379.
36. Orth, P. M. R., J. C. Hesketh, …, D. Fedida. 2006. RSD1235 blocks late I_{Na} and suppresses early afterdepolarizations and torsades de pointes induced by class III agents. *Cardiovasc. Res.* 70:486–496.
37. Spencer, C. I., S. Baba, …, B. R. Conklin. 2014. Calcium transients closely reflect prolonged action potentials in I_{PSC} models of inherited cardiac arrhythmia. *Stem Cell Rev.* 3:269–281.
38. Morotti, S., A. G. Edwards, …, E. Grandi. 2014. A novel computational model of mouse myocyte electrophysiology to assess the synergy between Na^+ loading and CaMKII. *J. Physiol.* 592:1181–1197.
39. Cranefield, P. F. 1977. Action potentials, afterpotentials, and arrhythmias. *Circ. Res.* 41:415–423.
40. Rosen, M. R. 2009. A short, biased history of triggered activity. *Hellenic J. Cardiol.* 50:170–178.
41. Zeng, J., and Y. Rudy. 1995. Early afterdepolarizations in cardiac myocytes: mechanism and rate dependence. *Biophys. J.* 68:949–964.
42. Clancy, C. E., and Y. Rudy. 1999. Linking a genetic defect to its cellular phenotype in a cardiac arrhythmia. *Nature.* 400:566–569.
43. Clancy, C. E., and Y. Rudy. 2002. Na^+ channel mutation that causes both Brugada and long-QT syndrome phenotypes: a simulation study of mechanism. *Circulation.* 105:1208–1213.
44. Tran, D. X., D. Sato, …, Z. Qu. 2009. Bifurcation and chaos in a model of cardiac early afterdepolarizations. *Phys. Rev. Lett.* 102:258103.
45. Vandersickel, N., I. V. Kazbanov, …, A. V. Panfilov. 2014. A study of early afterdepolarizations in a model for human ventricular tissue. *PLoS ONE.* 9:e84595.

46. Xie, Y., E. Grandi, …, D. M. Bers. 2013. β-adrenergic stimulation activates early afterdepolarizations transiently via kinetic mismatch of PKA targets. *J. Mol. Cell. Cardiol.* 58:153–161.

47. Fujiwara, K., H. Tanaka, …, T. Takamatsu. 2008. Burst emergence of intracellular Ca^{2+} waves evokes arrhythmogenic oscillatory depolarization via the Na^{+}-Ca^{2+} exchanger: simultaneous confocal recording of membrane potential and intracellular Ca^{2+} in the heart. *Circ. Res.* 103:509–518.

48. Wasserstrom, J. A., Y. Shiferaw, …, G. L. Aistrup. 2010. Variability in timing of spontaneous calcium release in the intact rat heart is determined by the time course of sarcoplasmic reticulum calcium load. *Circ. Res.* 107:1117–1126.

49. Shiferaw, Y., G. L. Aistrup, and J. A. Wasserstrom. 2012. Intracellular Ca^{2+} waves, afterdepolarizations, and triggered arrhythmias. *Cardiovasc. Res.* 95:265–268.

50. Ter Keurs, H. E. D. J., and P. A. Boyden. 2007. Calcium and arrhythmogenesis. *Physiol. Rev.* 87:457–506.

51. Nivala, M., C. Y. Ko, …, Z. Qu. 2012. Criticality in intracellular calcium signaling in cardiac myocytes. *Biophys. J.* 102:2433–2442.

52. Nivala, M., C. Y. Ko, …, Z. Qu. 2013. The emergence of subcellular pacemaker sites for calcium waves and oscillations. *J. Physiol.* 591:5305–5320.

53. Maruyama, M., B. Joung, …, P. S. Chen. 2010. Diastolic intracellular calcium-membrane voltage coupling gain and postshock arrhythmias: role of Purkinje fibers and triggered activity. *Circ. Res.* 106:399–408.

54. Pogwizd, S. M., K. Schlotthauer, …, D. M. Bers. 2001. Arrhythmogenesis and contractile dysfunction in heart failure: roles of sodium-calcium exchange, inward rectifier potassium current, and residual β-adrenergic responsiveness. *Circ. Res.* 88:1159–1167.

55. Qu, Z., and D. Chung. 2012. Mechanisms and determinants of ultralong action potential duration and slow rate-dependence in cardiac myocytes. *PLoS ONE.* 7:e43587.

56. Xie, Y., L. T. Izu, …, D. Sato. 2014. Arrhythmogenic transient dynamics in cardiac myocytes. *Biophys. J.* 106:1391–1397.

57. Chang, M. G., C. Y. Chang, …, M. R. Abraham. 2012. Dynamics of early afterdepolarization-mediated triggered activity in cardiac monolayers. *Biophys. J.* 102:2706–2714.

58. Maltsev, V. A., N. Silverman, …, A. I. Undrovinas. 2007. Chronic heart failure slows late sodium current in human and canine ventricular myocytes: implications for repolarization variability. *Eur. J. Heart Fail.* 9:219–227.

59. Guo, D., L. Young, …, G. X. Yan. 2008. Calcium-activated chloride current contributes to action potential alternans in left ventricular hypertrophy rabbit. *Am. J. Physiol. Heart Circ. Physiol.* 295:H97–H104.

60. Chua, S. K., P. C. Chang, …, P. S. Chen. 2011. Small-conductance calcium-activated potassium channel and recurrent ventricular fibrillation in failing rabbit ventricles. *Circ. Res.* 108:971–979.

61. Soeller, C., and M. B. Cannell. 1999. Examination of the transverse tubular system in living cardiac rat myocytes by 2-photon microscopy and digital image-processing techniques. *Circ. Res.* 84:266–275.

62. Baddeley, D., I. D. Jayasinghe, …, C. Soeller. 2009. Optical single-channel resolution imaging of the ryanodine receptor distribution in rat cardiac myocytes. *Proc. Natl. Acad. Sci. USA.* 106:22275–22280.

63. Chen, W., R. Wang, …, S. R. W. Chen. 2014. The ryanodine receptor store-sensing gate controls Ca^{2+} waves and Ca^{2+}-triggered arrhythmias. *Nat. Med.* 20:184–192.

64. Cheng, H., M. R. Lederer, …, M. B. Cannell. 1996. Calcium sparks and $[Ca^{2+}]_i$ waves in cardiac myocytes. *Am. J. Physiol.* 270:C148–C159.

65. DelPrincipe, F., M. Egger, and E. Niggli. 1999. Calcium signaling in cardiac muscle: refractoriness revealed by coherent activation. *Nat. Cell Biol.* 1:323–329.

66. Sobie, E. A., L. S. Song, and W. J. Lederer. 2005. Local recovery of Ca^{2+} release in rat ventricular myocytes. *J. Physiol.* 565:441–447.

67. Ramay, H. R., O. Z. Liu, and E. A. Sobie. 2011. Recovery of cardiac calcium release is controlled by sarcoplasmic reticulum refilling and ryanodine receptor sensitivity. *Cardiovasc. Res.* 91:598–605.

68. Belevych, A. E., D. Terentyev, …, S. Györke. 2012. Shortened Ca^{2+} signaling refractoriness underlies cellular arrhythmogenesis in a post-infarction model of sudden cardiac death. *Circ. Res.* 110:569–577.

69. Wasserstrom, J. A., R. Sharma, …, G. L. Aistrup. 2009. Ranolazine antagonizes the effects of increased late sodium current on intracellular calcium cycling in rat isolated intact heart. *J. Pharmacol. Exp. Ther.* 331:382–391.

70. Swaminathan, P. D., A. Purohit, …, M. E. Anderson. 2012. Calmodulin-dependent protein kinase II: linking heart failure and arrhythmias. *Circ. Res.* 110:1661–1677.

71. Huffaker, R. B., J. N. Weiss, and B. Kogan. 2007. Effects of early afterdepolarizations on reentry in cardiac tissue: a simulation study. *Am. J. Physiol. Heart Circ. Physiol.* 292:H3089–H3102.

72. Sato, D., L. H. Xie, …, Z. Qu. 2009. Synchronization of chaotic early afterdepolarizations in the genesis of cardiac arrhythmias. *Proc. Natl. Acad. Sci. USA.* 106:2983–2988.

Voltage-Calcium Coupling in the Genesis of Early and Delayed Afterdepolarizations in Cardiac Myocytes

Zhen Song, Christopher Y. Ko, Michael Nivala, James N. Weiss, Zhilin Qu

Supplemental Methods

A. Myocyte experiments

Myocyte Isolation. Mouse ventricular myocytes were isolated enzymatically as described previously (2). Briefly, C57Bl/6 mice (6-8 weeks) were injected intraperitoneally with 800 μl heparin (5,000 units/ml) 20-30 minutes before anesthetization and sacrifice with isoflurane (Phoenix Pharmaceuticals, Inc.). Hearts were quickly excised by thoracotomy and retrogradely perfused on a Langendorff apparatus maintained at 37°C. Enzyme digestion step consisted of perfusing Tyrode's solution containing 1 mg/ml collagenase (Type II; Worthington) and 2.8 mg/ml protease (Type XIV, Sigma) for 13-15 minutes. Myocytes were separated from digested ventricles by gentle mechanical dissociation and used within 4-6 hours. The modified Tyrode's solution contained the following (mmol/L): 136 NaCl, 5.4 KCl, 0.33 NaH_2PO_4, 1.0 $MgCl_2$, 10 HEPES, and 10 glucose; pH 7.4 (KOH). All chemicals were purchased from Sigma unless indicated otherwise. All procedures comply with UCLA Animal Research Committee policies.

Patch Clamp Recordings. APs from isolated myocytes were recorded in the current clamp mode using the perforated patch technique with Amphotericin B (240 μg/ml), as previously described (6, 7). Borosilicate glass electrodes (tip resistance 1.5-3 MΩ) were filled with internal solution containing (in mmol/L) 110 K-Aspartate, 30 KCl, 5 NaCl, 10 HEPES, 0.1 EGTA, 5 MgATP, 5 creatine phosphate, and 0.1 cAMP; pH 7.2 (KOH). The standard bath Tyrode's solution contained (in mmol/L): 136 NaCl, 5.4 KCl, 0.33 NaH_2PO_4, 1.0 $MgCl_2$, 10 HEPES, 1.8 $CaCl_2$, and 10 glucose; pH 7.4 (KOH). Extracellular [Ca] was raised to 2.7 mmol/L to facilitate EADs and DADs. APs were elicited with square current pulses of 2 ms duration and twice threshold amplitude. Data were acquired with an Axopatch 200A patch-clamp amplifier and Digidata 1200 acquisition board driven by pCLAMP 9.0 software (Axon Instruments, Inc.). Corrections were made for liquid junction potentials. Signals were filtered at 1 kHz. All experiments were carried out at 37°C.

Calcium Imaging. Myocytes were incubated with fluorescent Ca indicator dye Fluo-4 AM (10 μM, Life Technologies) and nonionic surfactant Pluronic F-127 (0.02%, Life Technologies) in Tyrode's solution for 30 minutes at room temperature before imaging. Ca fluorescence in isolated myocytes was recorded using an inverted Nikon Diaphot microscope (60X objective, Olympus) equipped with a charge-coupled device (CCD)-based Photometrics Cascade 128+ camera (~120 frames/s, 128 x 128 pixels) operating under Imaging Workbench software (version 6.0, INDEC BioSystems). Voltage was concurrently recorded in patch-clamped myocytes. Pseudo-line scan images were generated from the acquired video data using ImageJ software (11).

B. Rabbit ventricular cell model

1. The spatial structure of ventricular myocyte model

The ventricular myocyte model is a three-dimensional object containing 19,305 (65×27×11) CRUs (FIGURE) with CRU spacing being 1.84 μm in the longitudinal direction and 0.9 μm in the transverse direction, corresponding to a dimension 121 μm × 25 μm × 11 μm. The CRUs are coupled via Ca diffusion in the cytosolic space and SR. The model was modified from the one developed by Restrepo et al. (12). The details of the model are described in the sections below. Briefly, each CRU contains five sub-volumes with defined volume ratios (right panel in FIG.A): network SR (NSR), junctional SR (JSR), dyadic space (DS), sub-membrane space (SUB), and cytosolic space (CYTO). Ca from extracellular space enters into DS via LCCs and is released from the JSR to DS via RyRs. Each CRU has a cluster of 100 RyR channels associated with a cluster of 12 LCCs, both simulated using random Markov transitions. Ca is extruded from the SUB space via NCX and taken up into the NSR from CYTO via SERCA pump. Ca diffuses freely between the SR sub-volumes and between the cytosolic sub-volumes. CRUs are coupled via Ca diffusion between neighboring NSR spaces, SUB

spaces, and CYTO spaces, respectively. No Ca diffusion exists directly between neighboring JSR spaces or between neighboring DS spaces.

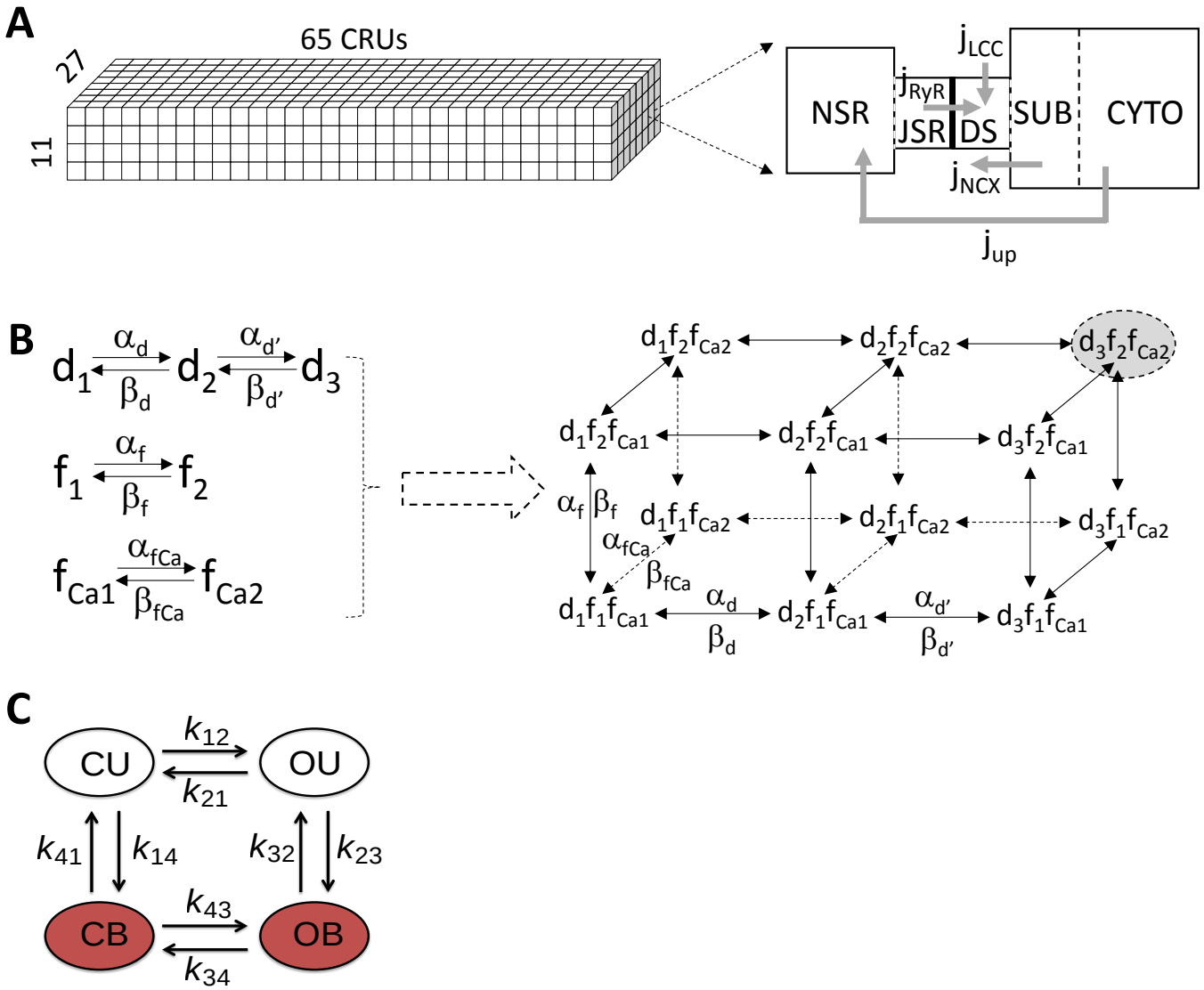

FIGURE. **Schematics of the computer AP/Ca cycling model**. **A**. Schematic diagrams of 3D structure of the cell model (left) and the CRU model (right). **B**. The modified $I_{Ca,L}$ model. Left: the Hodgkin-Huxley (HH) scheme. Right: the equivalent Markov scheme of the HH scheme. **C**. The 4-state RyR model.

However, a directly randomized version of the HH-type formulation is not appropriate for an LCC because the maximum open probability of an LCC is 100% in the HH-type model at high voltages, whereas that of real channels is much smaller (~5%). To reduce the open probability, we added a new state (d_3 in FIG.B) to the d gate of the HH-type model, with d_3 being the activated state. The transitions rates α_d, β_d, α_f, and β_f are the same as in the Luo and Rudy model (13). The rate constants for Ca-dependent inactivation were modified to account for the fact that Ca concentration in the DS space, which is much higher than the bulk cytosolic Ca concentration, was used to mediate LCC inactivation. The steady state of d_3 (the steady-state activation curve) is:

$$d_{3\infty} = \frac{\alpha_d}{\alpha_d + \frac{\beta_{d'}}{\alpha_{d'}}(\alpha_d + \beta_d)}$$

Since the open probability is small, i.e., $\frac{\beta_{d'}}{\alpha_{d'}} >> 1$, then $d_{3\infty} \approx \frac{\alpha_{d'}}{\beta_{d'}} \frac{\alpha_d}{\alpha_d + \beta_d}$, which is a rescale of the original model. Therefore, by shifting the voltage dependence of α_d and β_d or α_f and β_f, the window $I_{Ca,L}$ can be changed directly without affecting other properties of the channel. The right panel of FIG.B shows the equivalent Markov scheme of the LCC of the modified HH-type model.

2. Voltage and ionic currents

The differential equation for membrane voltage is

$$\frac{dV}{dt} = -\frac{1}{C_m}(I_{ion} + I_{stim})$$

where $C_m = 1\ \mu F/cm^2$ is the cell membrane capacitance, I_{stim} is the stimulus current pulse which was set as -40 $\mu A/cm^2$ and duration 1 ms, and I_{ion} is the total membrane current density, which is described by

$$I_{ion} = I_{Na} + I_{K1} + I_{Kr} + I_{Ks} + I_{to,f} + I_{to,s} + I_{NaK} + I_{Ca,L} + I_{NCX}$$

The mathematical formulations of the ionic currents are detailed in following sub-sections and their conductance are listed in Table S1. The physical constants and ion concentrations are listed in Table S2.

Table S1. Ionic current conductance

Parameter	Description	Value
g_{Na}	I_{Na} conductance	12.0 mS/μF
$g_{to,f}$	$I_{to,f}$ conductance	0.11 mS/μF
$g_{to,s}$	$I_{to,s}$ conductance	0.04 mS/μF
g_{K1}	I_{K1} conductance	0.3 mS/μF
g_{Kr}	I_{Kr} conductance	0.0125 mS/μF
g_{Ks}	I_{Ks} conductance	0.1386 mS/μF
g_{Nak}	I_{NaK} conductance	1.5 mS/μF

Table S2. Physical constants and ionic concentrations

Parameter	Description	Value
F	Faraday constant	96.5 C/mmol
R	Universal gas constant	8.315 $Jmol^{-1}K^{-1}$
T	Temperature	308 K
$[Na]_o$	External sodium concentration	136 mM
$[K]_o$	External potassium concentration	5.4 mM
$[K]_i$	Internal potassium concentration	140 mM
$[Ca]_o$	External calcium concentration	1.8 mM

2.1. Sodium current (I_{Na})

$$I_{Na} = g_{Na} m^3 hj(V - E_{Na}),$$

$$E_{Na} = \frac{RT}{F} \ln\left(\frac{[Na]_o}{[Na]_i}\right),$$

$$\frac{dh}{dt} = \alpha_h(1-h) - \beta_h h,$$

$$\frac{dj}{dt} = \alpha_j(1-j) - \beta_j j,$$

$$\frac{dm}{dt} = \alpha_m(1-m) - \beta_m m,$$

$$\alpha_m = 0.32\frac{V+47.13}{1-e^{-0.1(V+47.13)}},$$
$$\beta_m = 0.08e^{-\frac{V}{11}},$$

For $V \geq -40\ mV$,

$$\alpha_h = 0,$$
$$\alpha_j = 0,$$
$$\beta_h = \frac{1}{0.13\left(1+e^{\frac{V+10.66}{-11.1}}\right)},$$
$$\beta_j = 0.3\frac{e^{-2.535\times10^{-7}V}}{1+e^{-0.1(V+32)}},$$

For $V \leq -40\ mV$,

$$\alpha_h = 0.135e^{\frac{V+80}{-6.8}},$$
$$\beta_h = 3.56e^{0.079V} + 3.1\times10^5 e^{0.35V},$$
$$\alpha_j = \frac{(-127140e^{0.2444V} - 0.03474e^{-0.04391V})\times(V+37.78)}{1+e^{0.311(V+79.23)}},$$
$$\beta_j = \frac{0.1212e^{-0.01052V}}{1+e^{-0.1378(V+40.14)}}.$$

2.2. L-type Ca channel model and whole-cell $I_{Ca,L}$

The Ca channel model was modified as described in detail in Section 1. The opening of individual LCCs is simulated by a stochastic 12-state Markov model (panel B in FIGURE). Each CRU is assumed to have N_L LCCs under control condition. The Ca flux into the proximal space (dyadic space) of a CRU (the (m, n, k)th CRU in cell) is given by

$$\bar{I}_{Ca,L}(m,n,k) = i_{Ca,L}(m,n,k)L(m,n,k),$$

where $L \leq N_L$ is the number of open LCCs in the CRU, and $i_{Ca,L}$ is the single channel current of the CRU which is:

$$i_{Ca,L}(m,n,k) = \frac{4P_{Ca}zF\left(\gamma_i\, c_p(m,n,k)e^{2z} - \gamma_o[Ca]_o\right)}{e^{2z}-1},$$
$$z = \frac{VT}{RT}.$$

c_p(m,n,k) is the Ca concentration in the corresponding proximal space of the CRU. Therefore, the whole-cell L-type Ca current ($I_{Ca,L}$) is summation of the Ca currents of CRUs in the cell, i.e.,

$$I_{Ca,L} = \sum_{m,n,k=1}^{M,N,K} \bar{I}_{Ca,L}(m,n,k)$$

where M, N, and K are the dimensions of the CRU network forming the cell.

The transition rates between different states of the LCC model are:

$$\alpha_d = \frac{d_\infty}{\tau_d}, \qquad \beta_d = \frac{1-d_\infty}{\tau_d}$$

where

$$d_\infty = \frac{1}{1+e^{-\frac{V-5}{6.24}}},$$
$$\tau_d = \frac{1-e^{-\frac{V-5}{6.24}}}{0.035(V-5)}\, d_\infty.$$

$$\alpha_f = \frac{f_\infty}{\tau_f}, \qquad \beta_f = \frac{1 - f_\infty}{\tau_f}$$

where

$$f_\infty = \frac{1}{1 + e^{\frac{V+32.06}{8.6}}},$$

$$\tau_f = \frac{1}{0.0197e^{-[0.0337(V+7)]^2} + 0.02}.$$

$$\alpha_{fCa} = \frac{f_{Ca\infty}}{\tau_{fCa}}, \qquad \beta_{fCa} = \frac{1 - f_{Ca\infty}}{\tau_{fCa}}$$

where

$$f_{Ca\infty} = \frac{1}{1 + \left(\frac{c_p}{\bar{c}_p}\right)^2}.$$

$\alpha_{d'}$ and $\beta_{d'}$ are constants (Table S3). The parameters are listed in Table S3.

Table S3. L-type Ca current parameters

Parameter	Description	Value
P_{Ca}	L-type channel permeability	11.9 μmolC^{-1}ms^{-1}
γ_i, γ_o	Activity coefficient of Ca	0.341
N_L	Number of LCCs in each CRU	12
$\bar{c}_p$	Threshold of Ca-dependent inactivation	6 μM
τ_{fCa}	Time constant of Ca-dependent inactivation	15 ms
$\alpha_{d'}$	Transition rate from d_2 to d_3	0.3 ms^{-1}
$\beta_{d'}$	Transition rate from d_3 to d_2	6 ms^{-1}

2.3. Sodium-calcium exchange current (I_{NCX})

The Na-Ca exchange are spatially distributed in the CRUs, which are functions of Ca concentrations of the local sub-membrane spaces (c_s). For the (m,n,k)th CRU, the Na-Ca change current is:

$$\bar{I}_{NCX}(m,n,k) = \frac{K_a \nu_{NaCa}\left(e^{\eta z}[Na]_i[Ca]_o - e^{(\eta-1)z}[Na]_o^3 c_s(m,n,k)\right)}{(t_1 + t_2 + t_3)(1 + k_{sat}e^{(\eta-1)z})},$$

where

$$t_1 = K_{mCai}\,[Na]_o^2\left[1 + \left(\frac{[Na]_i}{K_{mNai}}\right)^3\right],$$

$$t_2 = K_{mNao}^3 c_s(m,n,k)(1 + \frac{c_s(m,n,k)}{K_{mCai}})$$

$$t_3 = K_{mCao}^3[Na]_i^3 + [Na]_i^3[Ca]_o + [Na]_o^3 c_s(m,n,k),$$

$$K_a = \left[1 + \left(\frac{K_{da}}{c_s(n,m,k)}\right)^3\right]^{-1},$$

$$z = \frac{VF}{RT},$$

and the whole-cell I_{NCX} is:

$$I_{NCX} = \sum_{m,n,k=1}^{M,N,K} \bar{I}_{NCX}(m,n,k)$$

The parameters are listed in Table S4.

Table S4. Sodium-calcium exchange current parameters

Parameter	Value	Units
v_{NaCa}	7	μM ms^{-1}
$\mathrm{K_{mCai}}$	3.59	μM
$\mathrm{K_{mCao}}$	1.3	mM
$\mathrm{K_{mNai}}$	12.3	mM
$\mathrm{K_{mNao}}$	87.5	mM
$\mathrm{K_{da}}$	0.11	μM
$\mathrm{k_{sat}}$	0.27	
η	0.35	

2.4. Inward rectifier K current (I_{K1})

$$I_{K1} = g_{K1}\sqrt{\frac{[K]_o}{5.4}}\,\frac{A_{K1}}{A_{K1}+B_{K1}}(V-E_K),$$

$$A_{K1} = \frac{1.02}{1+e^{0.2385(V-E_K-59.215)}},$$

$$B_{K1} = \frac{0.49124e^{0.08032(V-E_K+5.476)} + e^{0.06175(V-E_K-594.31)}}{1+e^{-0.5143(V-E_K+4.753)}},$$

$$E_K = \frac{RT}{F}\ln\left(\frac{[K]_o}{[K]_i}\right).$$

2.5. The rapid component of the delayed rectifier K current (I_{Kr})

$$I_{Kr} = g_{Kr}\sqrt{\frac{[K]_o}{5.4}}\,x_{Kr}R(V)(V-E_K),$$

$$R(V) = \frac{1}{1+e^{\frac{V+33}{22.4}}},$$

$$\frac{dx_{Kr}}{dt} = \frac{x_{Kr}^{\infty}-x_{Kr}}{\tau_{Kr}},$$

$$x_{Kr}^{\infty} = \frac{1}{1 + e^{-\frac{V+50}{7.5}}},$$

$$\tau_{Kr} = \frac{1}{\frac{0.00138(V+7)}{1 - e^{-0.123(V+7)}} + \frac{0.00061(V+10)}{-1 + e^{0.145(V+10)}}},$$

2.6. The slow component of the delayed rectifier K current (I_{Ks})

$$I_{Ks} = g_{Ks} x_{s1} x_{s2} q_{Ks} (V - E_{Ks}),$$
$$q_{Ks} = 1 + \frac{0.8}{1 + \left(\frac{0.5}{c_i}\right)^3},$$

$$\frac{dx_{s1}}{dt} = \frac{x_s^{\infty} - x_{s1}}{\tau_{xs1}},$$

$$\frac{dx_{s2}}{dt} = \frac{x_s^{\infty} - x_{s2}}{\tau_{xs2}},$$

$$x_s^{\infty} = \frac{1}{1 + e^{-\frac{V-1.5}{16.7}}},$$

$$\tau_{xs1} = \frac{1}{\frac{0.0000719(V+30)}{1 - e^{-0.148(V+30)}} + \frac{0.00031(V+30)}{-1 + e^{0.0687(V+30)}}},$$

$$\tau_{xs2} = 4\tau_{xs1},$$

$$E_{Ks} = \frac{RT}{F} \ln\left(\frac{[K]_o + 0.01833[Na]_o}{[K]_i + 0.01833[Na]_i}\right).$$

2.7. The fast component of the outward K current ($I_{to,f}$)

$$I_{to,f} = g_{to,f} X_{to,f} Y_{to,f} (V - E_K),$$
$$X_{to,f}^{\infty} = \frac{1}{1 + e^{-\frac{V+3}{15}}},$$

$$Y_{to,f}^{\infty} = \frac{1}{1 + e^{\frac{V+33.5}{10}}},$$

$$\tau_{Xto,f} = 3.5 e^{-\left(\frac{V}{30}\right)^2} + 1.5,$$
$$\tau_{Yto,f} = \frac{20}{1 + e^{\frac{V+33.5}{10}}} + 20,$$

$$\frac{dX_{to,f}}{dt} = \frac{X_{to,f}^{\infty} - X_{to,f}}{\tau_{Xto,f}},$$

$$\frac{dY_{to,f}}{dt} = \frac{Y_{to,f}^{\infty} - Y_{to,f}}{\tau_{Yto,f}}.$$

2.8. The slow component of the outward K current ($I_{to,s}$)

$$I_{to,s} = g_{to,s} X_{to,s}\left(Y_{to,s} + 0.5R_s^{\infty}\right)(V - E_K),$$

$$R_s^{\infty} = \frac{1}{1 + e^{\frac{V+33.5}{10}}},$$

$$X_{to,s}^{\infty} = \frac{1}{1 + e^{-\frac{V+3}{15}}},$$

$$Y_{to,s}^{\infty} = \frac{1}{1 + e^{\frac{(V+33.5)}{10}}},$$

$$\tau_{Xto,s} = \frac{9}{1 + e^{\frac{V+3}{15}}} + 0.5,$$

$$\tau_{Yto,s} = \frac{3000}{1 + e^{\frac{V+60}{10}}} + 30,$$

$$\frac{dX_{to,s}}{dt} = \frac{X_{to,s}^{\infty} - X_{to,s}}{\tau_{Xto,s}},$$

$$\frac{dY_{to,s}}{dt} = \frac{Y_{to,s}^{\infty} - Y_{to,s}}{\tau_{Yto,s}}.$$

2.9. Sodium-potassium pump current (I_{NaK})

$$\sigma = \frac{e^{\frac{[Na]_o}{67.3}} - 1}{7},$$

$$f_{NaK} = \frac{1}{1 + 0.1245e^{-\frac{0.1VF}{RT}} + 0.0365\sigma e^{-\frac{VF}{RT}}},$$

$$I_{NaK} = g_{NaK} f_{NaK} \frac{1}{1 + \frac{12}{[Na]_i}} \times \frac{[K]_o}{[K]_o + 1.5}.$$

3. Intracellular Ca cycling

3.1. Differential equations for Ca cycling

The Ca cycling are described by the following differential equations [for an arbitrary CRU at a location (m,n,k) with the spatial location omitted in the equations]:

$$\frac{dc_i}{dt} = \beta_i(c_i)\left(I_{dsi}\frac{v_s}{v_i} - I_{up} + I_{leak} - I_{TCi} + I_{ci}\right),$$
$$\frac{dc_s}{dt} = \beta_s(c_s)\left(I_{dps}\frac{v_p}{v_s} + I_{NCX} - I_{dsi} - I_{TCs} + I_{cs}\right),$$
$$\frac{dc_p}{dt} = \beta_p(c_p)\left(I_{rel} + I_{Ca,L} - I_{dps}\right),$$
$$\frac{dc_{nsr}}{dt} = \left(I_{up} - I_{leak}\right)\frac{v_i}{v_{nsr}} - I_{tr}\frac{v_{jsr}}{v_{nsr}} + I_{cnsr},$$
$$\frac{dc_{jsr}}{dt} = \beta_{jsr}(c_{jsr})\left(I_{tr} - I_r\frac{v_p}{v_{jsr}}\right),$$

where c_i is the free Ca concentration in the bulk myoplasm, c_s is the free Ca concentration in a thin layer just below the cell membrane, c_p is the free Ca concentration in the proximal space (dyadic space), c_{jsr} is the free Ca concentration in the junctional SR, c_{nsr} is the free Ca concentration in the network SR, β terms account for instantaneous buffer in corresponding compartments using the rapid buffering approximation, I_{up} is the SERCA uptake current representing total flux into the NSR, I_{leak} is the leak current from NSR to cytosol, I_{NCX} is Na-Ca exchange current, $I_{Ca,L}$ is the L-type Ca influx, I_{rel} is the total Ca efflux from the JSR, I_{dsi}, I_{dps} and I_{tr} are the diffusion currents from adjacent compartments, I_{TCi} and I_{TCs} are the troponin C dynamic buffering currents in cytosol and submembrane spaces, I_{ci}, I_{cs} and I_{cnsr} are the diffusive currents between neighboring CRUs in the corresponding compartments. Note that currents are all local currents for a single CRU, for example, $I_{Ca,L}$ is the same as $\bar{I}_{Ca,L}(m,n,k)$ and I_{NCX} the same as $\bar{I}_{NCX}(m,n,k)$ in the expressions of the whole-cell currents described in the sections of ionic currents. The values of compartments volumes are listed in Table S5.

Table S5. Effective volumes of sub-space of a CRU

Parameter	Description	Value
v_i	Cytosolic volume	0.5 μm^3
v_s	Submembrane space volume	0.025 μm^3
v_p	Proximal space volume	0.00126 μm^3
v_{jsr}	JSR volume	0.02 μm^3
v_{nsr}	NSR volume	0.025 μm^3

3.2. Instantaneous cytosolic buffering

The factors $\beta_i(c_i)$ and $\beta_s(c_s)$ describe instantaneous buffering to Calmodulin, SR sites, Myosin (Ca^{2+}), and Myosin (Mg^{2+}). Note that the concentration of the proximal space rapidly equilibrates, so we do not require knowledge of the instantaneous buffers in the proximal space. The equation of $\beta_i(c_i)$ is

$$\beta_i(c_i) = \left[1 + \frac{\sum B_b K_b}{(c_i + K_b)^2}\right]^{-1},$$

where the sum is over the instantaneous cytosolic buffers Calmodulin, SR sites, Myosin (Ca^{2+}), and Myosin (Mg^{2+}), with buffer dissociation constants K_{CAM}, K_{SR}, K_{MCa}, and K_{MMg} and total concentration of buffering sites B_{CAM}, B_{SR}, B_{MCa}, and B_{MMg}, respectively. In addition to Calmodulin, instantaneous buffering in the submembrane space includes the subsarcolemmal sites of high affinity with total

concentration of sites and dissociation constant B_{SLH} and K_{SLH}, respectively. The parameters for instantaneous cytosolic buffering are in Table S6.

Table S6. Buffering parameters.

Parameter	Value	Units
K_{CAM}	7.0	μM
B_{CAM}	24.0	μM
K_{SR}	0.6	μM
B_{SR}	47.0	μM
K_{MCa}	0.033	μM
B_{MCa}	140.0	μM
K_{SLH}	0.3	μM
B_{SLH}	13.4	μM
B_T	70.0	μM
k_{on}^T	0.0327	(μM ms)$^{-1}$
k_{off}^T	0.0196	(ms)$^{-1}$

3.3. Troponin C buffering

I_{TCi} and I_{TCs} describe the rate of change in the concentration of Ca bound to Troponin C in the cytosolic and submembrane compartments, $[CaT]_i$ and $[CaT]_s$. These quantities satisfy

$$\frac{d[CaT]_i}{dt} = I_{TC_i},$$

with

$$I_{TC_i} = k_{on}^T c_i (B_T - [CaT]_i) - k_{off}^T [CaT]_i,$$

and analogous expressions apply for the submembrane compartments, replacing the subscript *i* by *s*. Here, k_{on}^T and k_{off}^T are the on- and off-rate constants for Ca Troponin C binding, and B_T is the total concentration of Troponin C buffering sites. The values of these parameters are listed in Table S6.

3.4. Instantaneous luminal buffering

$B_{jsr}(c_{jsr})$ describes instantaneous luminal Ca buffering to calsequestrin (CSQN). The expression of $\beta_{jsr}(c_{jsr})$ is

$$\beta(c) = \left(1 + \frac{K_c B_{CSQN} n(c) + \partial_c n(c)(cK_c + c^2)}{(K_c + c)^2}\right)^{-1},$$

where

$$n(c_{jsr}) = \widehat{M} n_M + (1 - \widehat{M}) n_D,$$

$$\widehat{M} = \frac{(1 + 8\rho B_{CSQN})^{\frac{1}{2}} - 1}{4\rho B_{CSQN}},$$

and

$$\rho(c_{jsr}) = \frac{\rho_\infty c_{jsr}^h}{K^h + c_{jsr}^h}.$$

The parameters for luminal buffering are in Table S7.

Table S7: Luminal buffering parameters.

Parameter	Description	Value
B_{CSQN}	Concentration of CSQN molecules	460 μM
K_C	Dissociation constant of CSQN	600 μM
n_M	Buffering capacity of CSQN monomers	15
n_D	Buffering capacity of CSQN dimers	35
ρ_∞	Asymptotic ratio of dimers to monomers	5000
K	Dimerization constant	850 μM
H	Dimerization exponent (steep)	23

3.5. SR Ca uptake current (I_{up})

$$I_{up} = \nu_{up}\left(\frac{\left(\frac{c_i}{K_i}\right)^H - \left(\frac{c_{nsr}}{K_{nsr}}\right)^H}{1 + \left(\frac{c_i}{K_i}\right)^H + \left(\frac{c_{nsr}}{K_{nsr}}\right)^H}\right).$$

The parameters are listed in Table S8.

Table S8. Uptake and leak current parameters.

Parameter	Value	Units
ν_{up}	0.3	μM ms^{-1}
K_i	0.3	μM
K_{NSR}	1700	μM
H	1.787	
g_{leak}	1.035×10^{-5}	ms^{-1}
K_{JSR}	500	μM

3.6. SR leak current (I_{leak})

$$I_{leak} = g_{leak}\left(\frac{c_{jsr}^2}{c_{jsr}^2 + K_{jsr}^2}\right)(c_{nsr} - c_i).$$

3.7. RyR release flux (I_{rel})

$$I_{rel} = J_{max}\, P_o\, \frac{c_{jsr} - c_p}{\nu_p},$$

where P_o is the fraction of RyR channels that are in the open state of RyRs. J_{max} is the maximum RyR flux strength. The parameters are listed in Table S9.

3.8. RyR model

The RyR model includes the following 4 states (Panel D in FIGURE): closed CSQN-unbound (CU), open CSQN-unbound (OU), open CSQN-bound (OB), and closed CSQN-bound (CB). The rates of transition are:

$$k_{12} = K_u c_p^2,$$

$$k_{14} = \frac{\widehat{M}\tau_b^{-1}B_{CSQN}}{B_{CSQN}^0},$$
$$k_{21} = \tau_c^{-1},$$
$$k_{23} = \frac{\widehat{M}\tau_b^{-1}B_{CSQN}}{B_{CSQN}^0},$$
$$k_{43} = K_b c_p^2,$$
$$k_{41} = \tau_u^{-1},$$
$$k_{34} = \tau_c^{-1},$$
$$k_{32} = \frac{k_{41}k_{12}}{k_{43}}.$$

The parameters are listed in Table S9. Note that B_{CSQN}/B_{CSQN}^0 is only different from 1 when the CSQN concentration is modified.

Table S9. SR release current and RyR model parameters

Parameter	Description	Value
J_{max}	Maximum RyR flux strength	1.47×10^{-2} $\mu m^3 ms^{-1}$
K_u	CSQN-unbound opening rate	3.8×10^{-4} $\mu M^{-2} ms^{-1}$
K_b	CSQN-bound opening rate	1×10^{-5} $\mu M^{-2} ms^{-1}$
τ_u	CSQN-unbinding timescale	700.0 ms
τ_b	CSQN-binding timescale	10.0 ms
τ_c	RyR closing timescale	1.0 ms
B_{CSQN}^0	Normal CSQN concentration	460 μM

3.9. Nearest-neighbor diffusive currents

The diffusive currents in cytosol, submembrane and NSR are given by

$$I_{ci}^{(n)} = \sum \left(\frac{c_i^{(m)} - c_i^{(n)}}{\tau_{mn}} \right),$$

where the sum is over the six nearest neighbors. The values of the timescales (τ_{mn}) are listed in Table S10.

Table S10: Parameters of Ca Diffusion

Parameter	Description	Value
τ_i^T	Transverse cytosolic	2.93 ms
τ_i^L	Longitudinal cytosolic	2.32 ms
τ_{nsr}^T	Transversal NSR	7.2 ms
τ_{nsr}^L	Longitudinal NSR	24.0 ms
τ_s^T	Transversal submembrane	1.42 ms
τ_s^L	Longitudinal submembrane	3.4 ms

C. Mouse ventricular cell model

We used the same spatial CRU structure and distribution as the rabbit ventricular cell model described above but substituted the ionic currents of mouse ventricular myocytes formulated by Morotti et al (5) except $I_{Ca,L}$ which was the same as in the rabbit ventricular cell model but a 65% increase in conductance, i.e.,

P_{Ca}=19.635 μmolC^{-1}ms^{-1}. The total ionic current is

$$I_{ion} = I_{Na} + I_{Na,L} + I_{Nabk} + I_{K1} + I_{Kr} + I_{to,f} + I_{NaK} + I_{Ca,L} + I_{Cabk} + I_{NCX} + I_{Kslow1} + I_{Kslow2} + I_{ss}$$

The details of the ionic currents are described below. The parameters are the same as in the Morotti et al unless specified.

Sodium current (I_{Na})

$$I_{Na} = g_{Na} m^3 hj(V - E_{Na}) ,$$

$$E_{Na} = \frac{RT}{F} \ln\left(\frac{[Na]_o}{[Na]_i}\right),$$

$$\frac{dh}{dt} = \alpha_h(1 - h) - \beta_h h ,$$

$$\frac{dj}{dt} = \alpha_j(1 - j) - \beta_j j ,$$

$$\frac{dm}{dt} = \alpha_m(1 - m) - \beta_m m ,$$

$$\alpha_m = 0.32 \frac{V + 47.13}{1 - e^{-0.1(V+47.13)}},$$

$$\beta_m = 0.08 e^{-\frac{V}{11}} ,$$

For $V \geq -40\ mV$,

$$\alpha_h = 0 ,$$

$$\alpha_j = 0 ,$$

$$\beta_h = \frac{0.66}{0.13\left(1 + e^{\frac{V+10.66}{-11.1}}\right)},$$

$$\beta_j = 0.3 \frac{e^{-2.535\times10^{-7}V}}{1 + e^{-0.1(V+32)}},$$

For $V \leq -40\ mV$,

$$\alpha_h = 0.135 e^{\frac{V+80}{-6.8}} ,$$

$$\beta_h = 3.92 e^{0.079(V-2)} + 3.1 \times 10^5 e^{0.35(V-2)} ,$$

$$\alpha_j = \frac{(-127140 e^{0.2444V} - 0.03474 e^{-0.04391V}) \times (V + 37.78)}{1 + e^{0.311(V+79.23)}},$$

$$\beta_j = \frac{0.1212e^{-0.01052V}}{1 + e^{-0.1378(V+40.14)}}.$$

Late sodium current ($I_{Na,L}$)

$$I_{Na,L} = g_{Na,L} m_L{}^3 h_L \left(V - E_{Na,L}\right),$$

$$E_{Na,L} = \frac{RT}{F} \ln\left(\frac{[Na]_o}{[Na]_i}\right),$$

$$h_{L,\infty} = \frac{1}{1 + \exp\left(\frac{V + 91}{6.1}\right)}$$

$$\tau_h = 4000\ ms$$

where m_L is the same as m in I_{Na}.

Background sodium current (I_{Nabk})

$$I_{Nabk} = g_{nabk}(V - E_{Na})$$

Inward rectifier potassium current (I_{K1})

$$I_{K1} = g_{K1} \sqrt{\frac{[K]_o}{5.4}}\ \frac{A_{K1}}{A_{K1} + B_{K1}} (V - E_K),$$

$$A_{K1} = \frac{1.02}{1 + e^{0.2385(V - E_K - 59.215)}},$$

$$B_{K1} = \frac{0.49124e^{0.08032(V - E_K + 5.476)} + e^{0.06175(V - E_K - 594.31)}}{1 + e^{-0.5143(V - E_K + 4.753)}},$$

$$E_K = \frac{RT}{F} \ln\left(\frac{[K]_o}{[K]_i}\right).$$

The rapid component of the delayed rectifier potassium current (I_{Kr})

$$I_{Kr} = g_{Kr} \sqrt{\frac{[K]_o}{5.4}}\ x_{Kr} R(V)(V - E_K),$$

$$R(V) = \frac{1}{1 + e^{\frac{V+33}{22.4}}},$$

$$\frac{dx_{Kr}}{dt} = \frac{x_{Kr}^{\infty} - x_{Kr}}{\tau_{Kr}},$$

$$x_{Kr}^{\infty} = \frac{1}{1 + e^{-\frac{V+50}{7.5}}},$$

$$\tau_{Kr} = \frac{1}{\frac{0.00138(V+7)}{1 - e^{-0.123(V+7)}} + \frac{0.00061(V+10)}{-1 + e^{0.145(V+10)}}},$$

The fast component of the transient outward potassium current ($I_{to,f}$)

$$I_{to,f} = g_{to,f} X_{to,f} Y_{to,f} (V - E_K),$$

$$X_{to,f}^{\infty} = \frac{1}{1 + e^{-\frac{V+3}{13}}},$$

$$Y_{to,f}^{\infty} = \frac{1}{1 + e^{\frac{V+48}{5}}},$$

$$\tau_{Xto,f} = 0.7e^{-\left(\frac{V+25}{30}\right)^2} + 0.08,$$

$$\tau_{Yto,f} = \frac{8}{1 + e^{\frac{V+60}{8}}} + 32e^{-\left(\frac{V+55}{16}\right)^2} + 10,$$

$$\frac{dX_{to,f}}{dt} = \frac{X_{to,f}^{\infty} - X_{to,f}}{\tau_{Xto,f}},$$

$$\frac{dY_{to,f}}{dt} = \frac{Y_{to,f}^{\infty} - Y_{to,f}}{\tau_{Yto,f}}.$$

Sodium-potassium pump current (I_{NaK})

$$\sigma = \frac{e^{\frac{[Na]_o}{67.3}} - 1}{7},$$

$$f_{NaK} = \frac{1}{1 + 0.1245e^{-\frac{0.1VF}{RT}} + 0.0365\sigma e^{-\frac{VF}{RT}}},$$

$$I_{NaK} = g_{NaK} f_{NaK} \frac{1}{1 + \frac{19}{[Na]_i}} \times \frac{[K]_o}{[K]_o + 1.5}.$$

L-type calcium current ($I_{Ca,L}$)

$I_{Ca,L}$ formulation is the same as in the rabbit ventricular cell model except that the activation kinetics is shifted to the negative voltage direction for 15 mV, i.e.,

$$d_\infty = \frac{1}{1+e^{-\frac{V+10}{6.24}}},$$

$$\tau_d = \frac{1-e^{-\frac{V+10}{6.24}}}{0.035(V+10)}\, d_\infty.$$

Background calcium leak current (I_{Cabk})

$$I_{Cabk} = g_{cabk}(V - E_{Ca})$$

Sodium-calcium exchange current (I_{NCX})

I_{NCX} formulation is the same as in the rabbit model with v_{NaCa}=3.6 pA/pF.

Slowly inactivating delayed rectifier potassium current ($I_{K,slow}$)

$$I_{kslow} = I_{kslow1} + I_{kslow2}$$

$$I_{kslow1} = g_{kslow1} x_{kslow1} y_{kslow1}(V - E_K)$$

$$I_{kslow2} = g_{kslow2} x_{kslow2} y_{kslow2}(V - E_K)$$

$$x_{kslowss} = \frac{1}{1+e^{\frac{V+15}{14}}}$$

$$\tau_{xkslow} = 0.95 + 0.05e^{-0.08V}$$

$$y_{kslowss} = \frac{1}{1+e^{\frac{V+48}{6.2}}}$$

$$\tau_{ykslow1} = 400 + 900e^{-\left(\frac{V+55}{16}\right)^2} - \frac{250}{1+e^{\frac{V+60}{8}}}$$

$$\tau_{ykslow2} = 400 + 900e^{-\left(\frac{V+55}{16}\right)^2} - \frac{550}{1+e^{\frac{V+60}{8}}}$$

$$\frac{dx_{kslow}}{dt} = \frac{x_{kslowss} - x_{kslow}}{\tau_{xkslow}},$$

$$\frac{dy_{kslow1}}{dt} = \frac{y_{kslowss} - y_{kslow1}}{\tau_{ykslow1}},$$

$$\frac{dy_{kslow2}}{dt} = \frac{y_{kslowss} - y_{kslow2}}{\tau_{ykslow2}},$$

where g_{Kslow1}=0.0352 nS/pF and g_{Kslow2}=0.028 nS/pF.

Non-inactivating steady-state current (I_{ss})

$$I_{ss} = g_{ss} x_{ss} (V - E_K),$$

where

$$x_{ssss} = x_{kslowss}$$

$$\tau_{xss} = 14 + 70e^{-\left(\frac{V+43}{30}\right)^2}$$

$$\frac{dx_{ss}}{dt} = \frac{x_{ssss} - x_{ss}}{\tau_{xss}}$$

D. Numerical methods

The differential equations for voltage and Ca concentrations of different compartments were numerically solved using an Euler method with a time step of 0.1 ms. The gating variables were integrated using the method by Rush and Larsen (14). The LCCs were simulated by a standard Monte Carlo method using the Markov model shown in FIGURE. The RyRs were simulated using an optimized method developed by Restrepo et al (12), which is equivalent to the binomial τ-leaping method (15). For all the simulations in this study, we pre-paced the cell model 50 beats to reach the steady state. All computer programs were coded in CUDA C, and simulations were carried out on a Graphical Processing Unit workstation with 2 intel Xeon E5-26640 processors and 4 Nvidia Tesla K20 GPUs. To simulate 1 s of electrical and Ca cycling activity, it takes ≈ 10 s of computational time.

Supplemental Figures

(Complex EAD behaviors observed in experiments from literature)

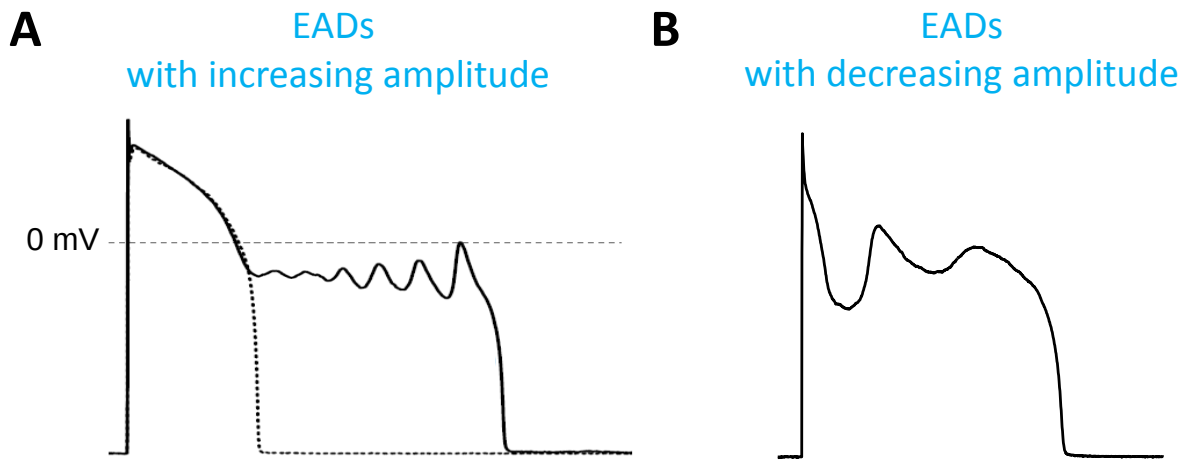

Fig.S1. **Complex EAD behaviors from experiments**. **A**. EADs with growing amplitude. From Liu et al (3). **B**. EADs with decreasing amplitude. From Xie et al (9).

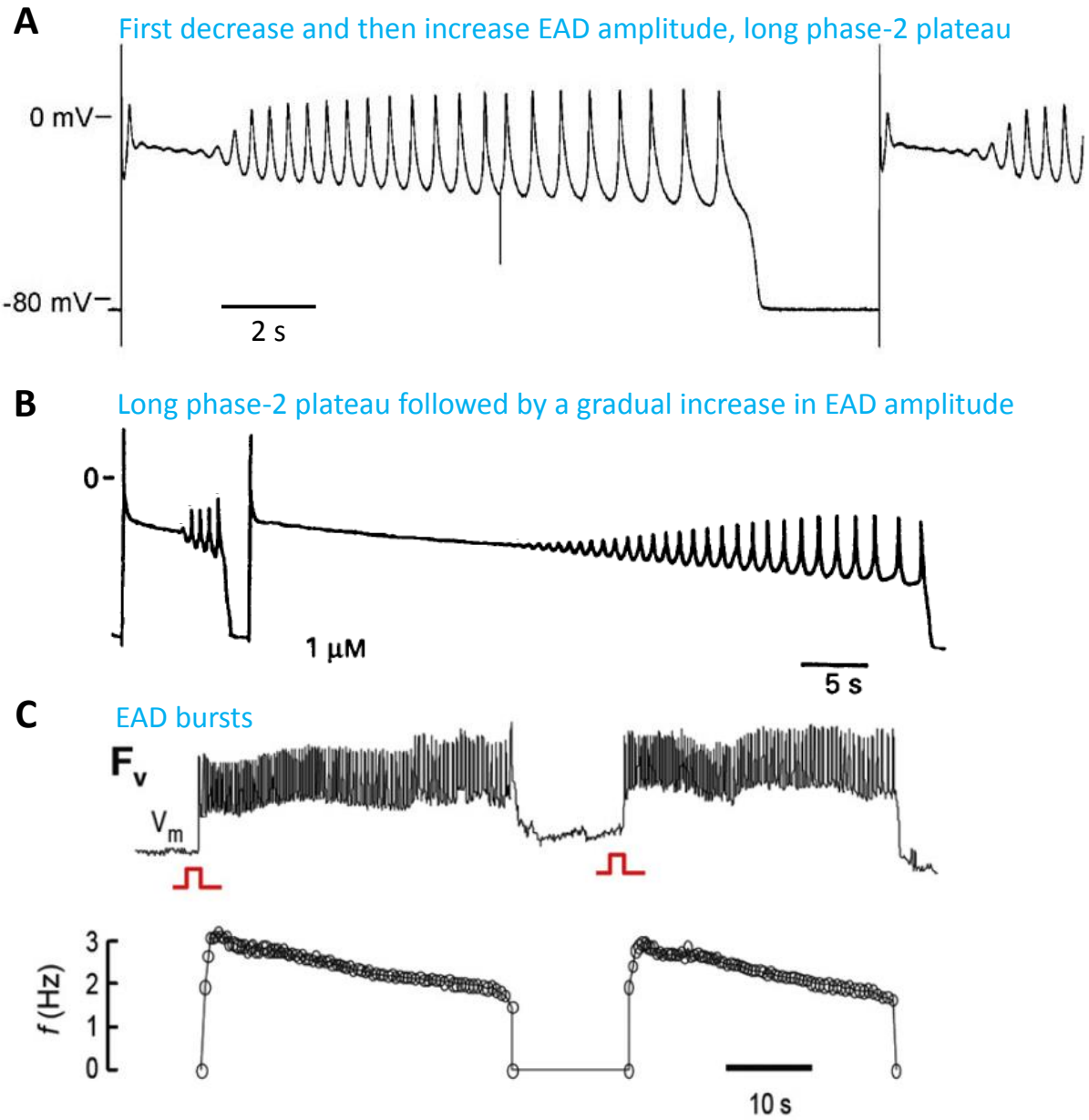

Fig.S2. Complex EAD behaviors from experiments. **A**. EADs with decreasing and then increasing amplitude and long phase-2 plateau. From Orth et al .(1). **B**. Long phase-2 plateau followed by EADs with growing amplitude. From Puisieux et al. (8). **C**. EAD bursts. Upper trace: optical voltage trace. Lower trace: Frequency of the EAD burst. From Change et al (10).

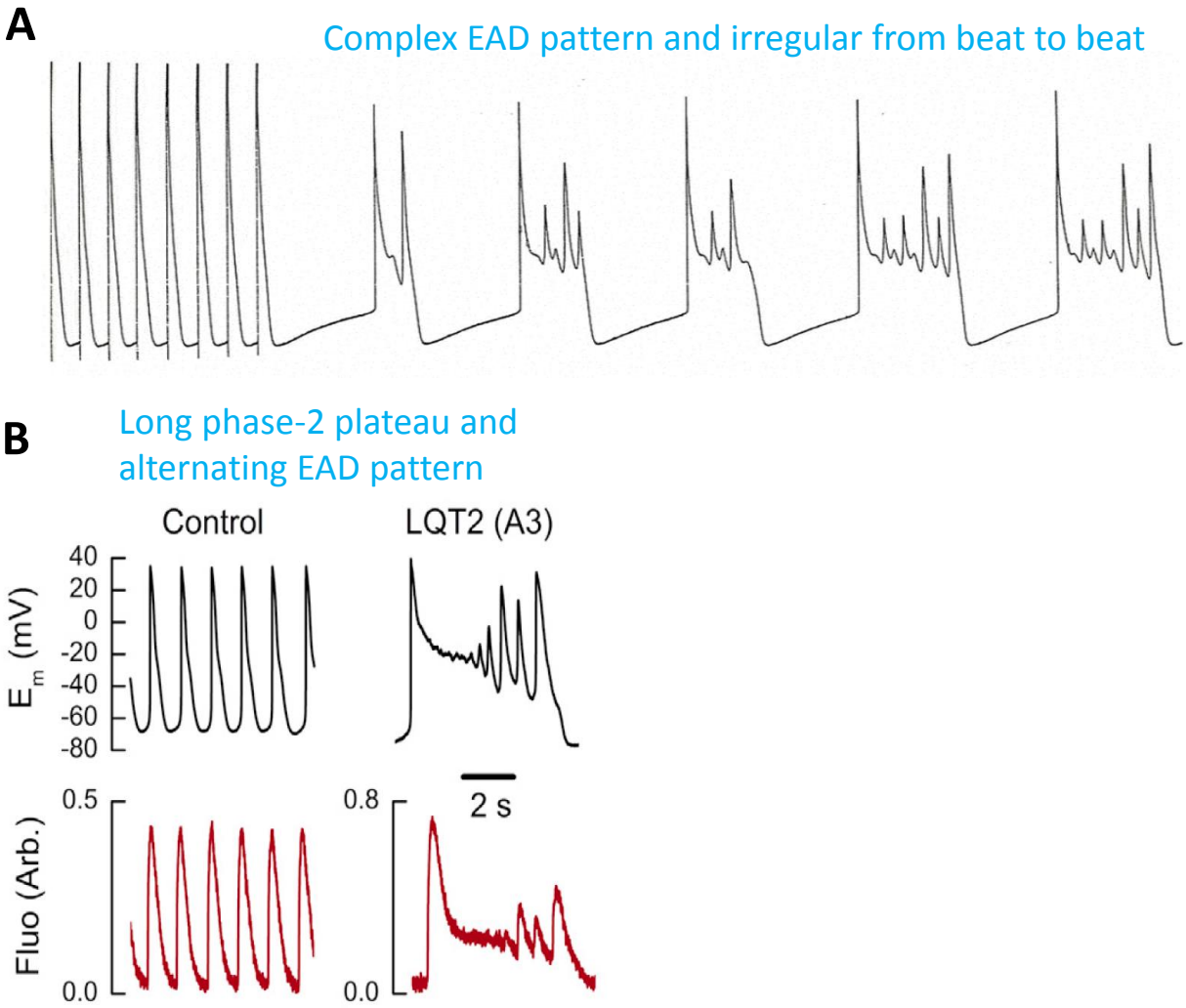

Fig.S3. Complex EAD behaviors from experiments. **A**. A recording from a dog Purkinje fiber showing complex EAD patterns and irregular beat-to-beat change (Courtesy of Robert Gilmour). **B.** Alternating EAD pattern following a long phase-2 plateau. During the phase-2 plateau, intracellular Ca is high without oscillation. From Spencer et al. (4).

Supplemental Results

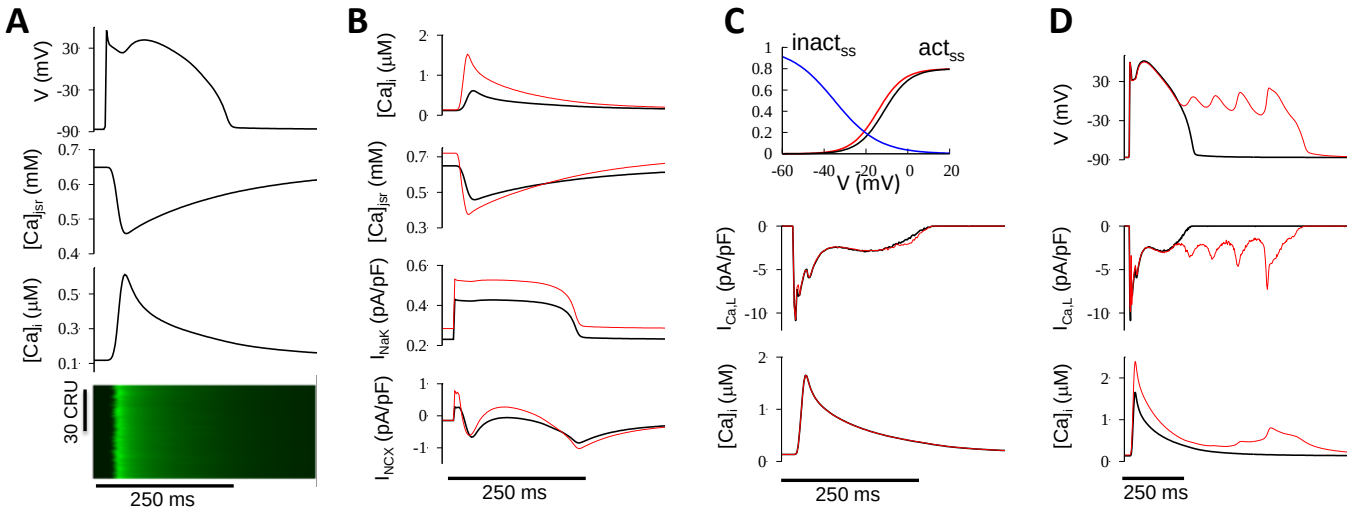

Fig. S4. **Model properties**. **A**. AP, $[Ca]_{SR}$, $[Ca]_i$, and a line scan of $[Ca]_i$ for the normal control model after steady state periodic pacing at PCL=2 s. **B**. $[Ca]_i$, $[Ca]_{SR}$, I_{NaK} and I_{NCX} for $[Na]_i$=7 mM (black) and 10 mM (red) obtained under voltage clamp condition using the AP in A and PCL=2 s. **C**. Upper panel: Steady-state activation (act_{ss}) and inactivation ($inact_{ss}$) curves of $I_{Ca,L}$. The red curve is the act_{ss} with 5 mV left-shift. Middle and lower panels: $I_{Ca,L}$ and $[Ca]_i$ before and after a 5 mV left-shift of $I_{Ca,L}$ steady-state activation curve under the same voltage clamp condition as in B. **D**. AP, $I_{Ca,L}$, and $[Ca]_i$ under free running condition (paced with PCL=2 s). The parameters are the same as in C. Note that under AP clamp conditions, 5 mV shift in act_{ss} has very small effect on $I_{Ca,L}$ and $[Ca]_i$ but under free running condition, EADs occur and the changes of $I_{Ca,L}$ and $[Ca]_i$ are large. The normal control model was used in panels A and B, and the L-type Ca channel open probability was increased (the same as in Fig.1 in the main text) in panels C and D.

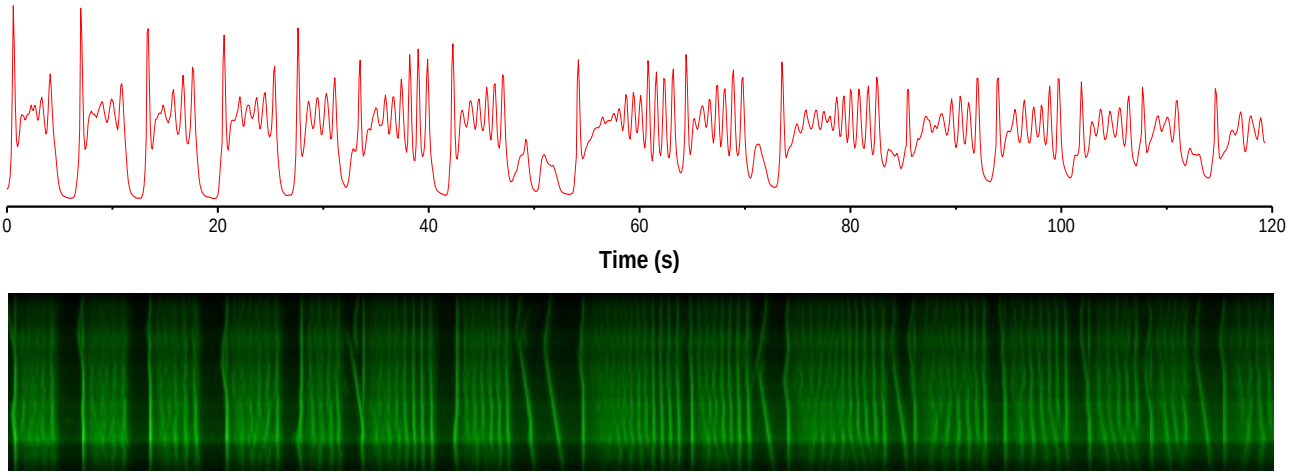

Fig.S5. The entire optical recording from which Fig.6B in the main text (from 40 s to around 72 s) was taken.

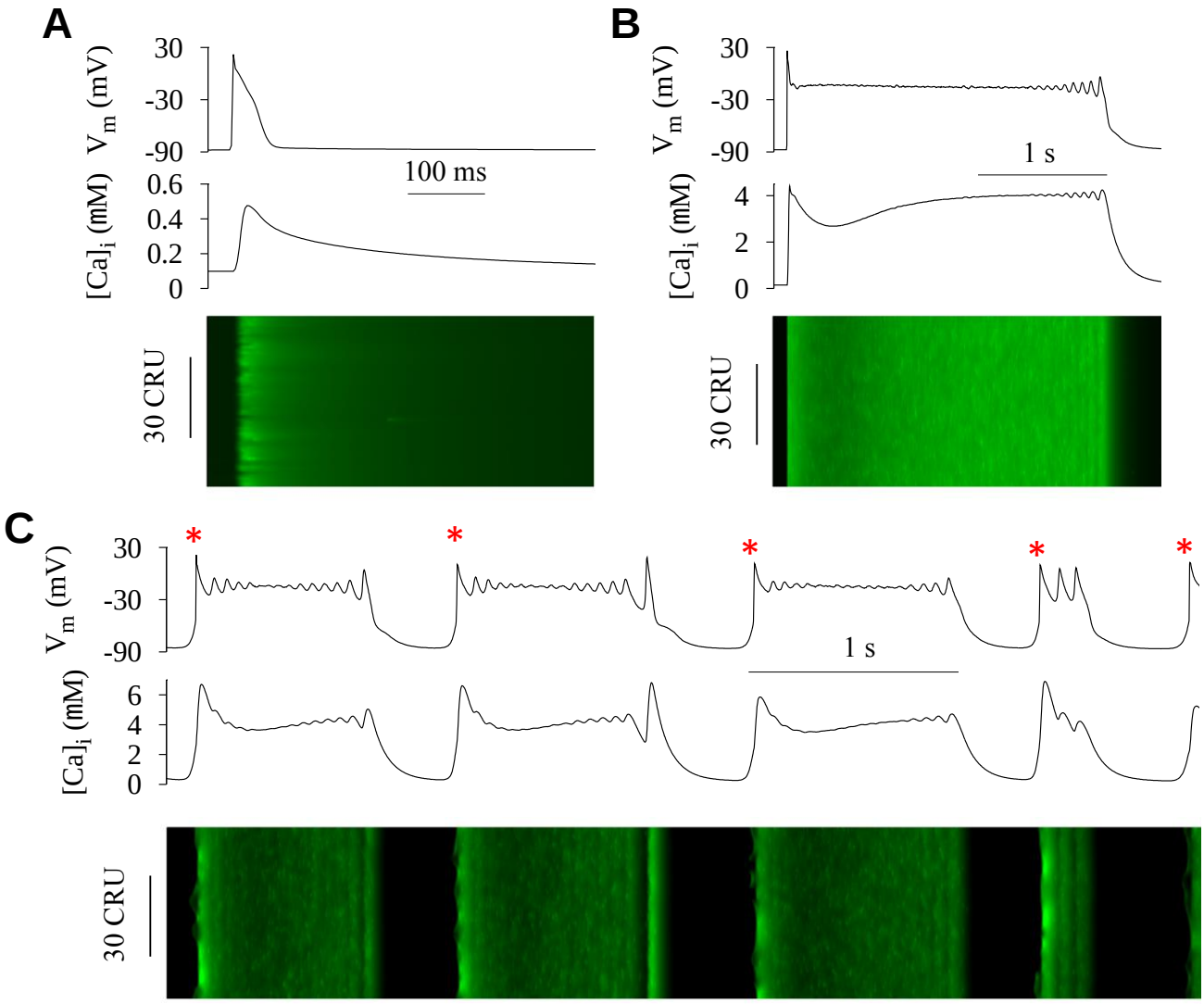

Fig.S6. Complex EAD-DAD dynamics in a mouse ventricular model. A. Time traces of voltage, whole cell averaged $[Ca]_i$ and the corresponding line scan for control conditions. PCL = 1 sec, and $[Ca]_o$ = 1 mM. **B**. pacing-induced EADs. $[Ca]_o$ = 2.7 mM and the maximum conductance of I_{NaL}=2.7 pA/pF. **C**. Spontaneous APs (indicated by asterisk) and EADs due to spontaneous Ca release. $[Ca]_o$=2.7 mM, the maximum conductance of I_{NaL}=1.2 pA/pF, with doubled the RyR leakiness, increased SERCA activity increased by 50%, and L-type Ca current by 50%. The mouse ventricular cell model were based on the model by Morrotti et al (5), as described in detail in the online supplemental text. The changes in B and C from control were under the assumption that Ca overload causes CaMKII activation which causes the corresponding changes to late I_{Na}, $I_{Ca,L}$, RyR, and SERCA.

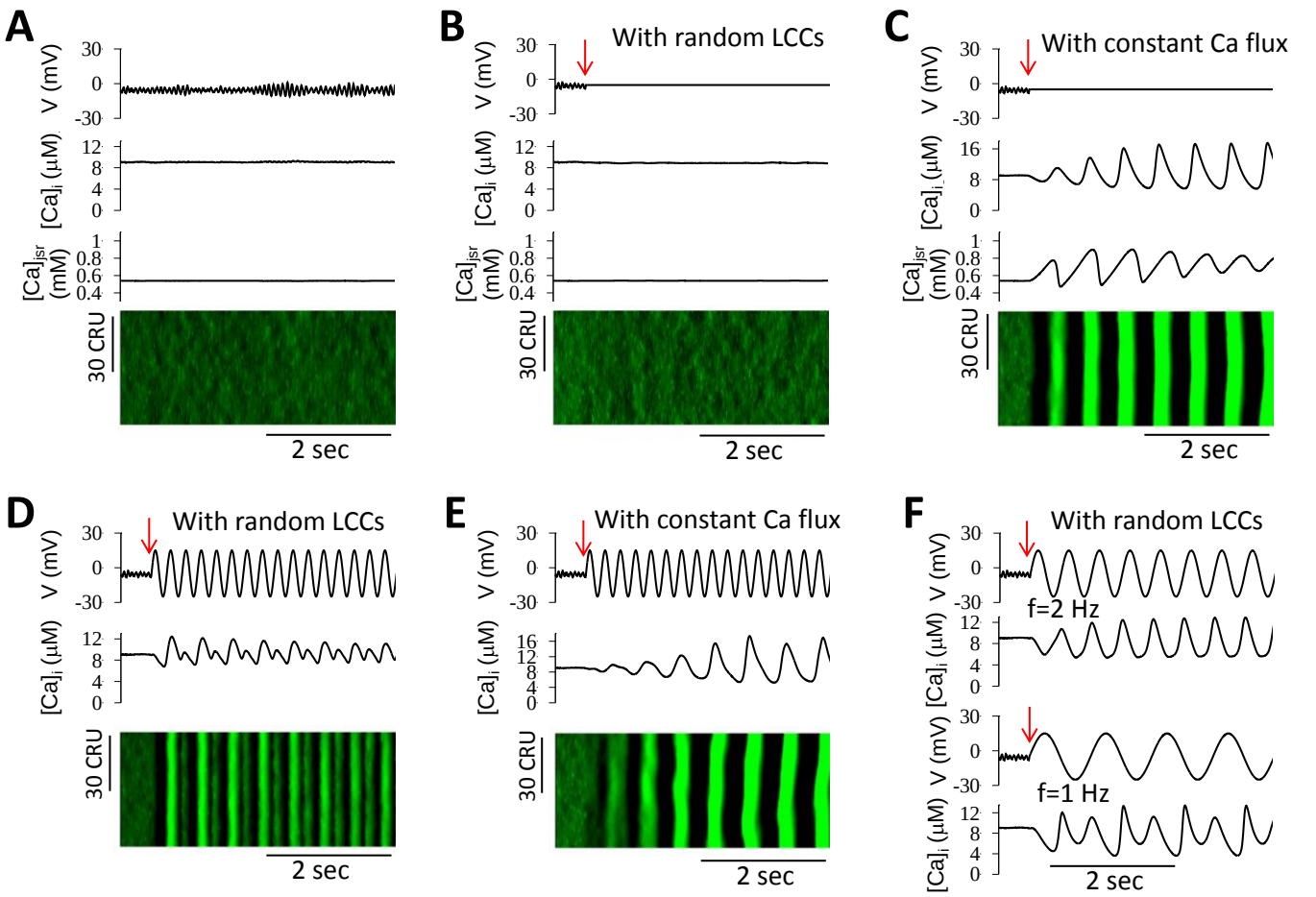

Fig.S7. **Interactions of voltage oscillations and Ca oscillations during repolarization failure**. Shown are voltage, $[Ca]_i$, and $[Ca]_{jsr}$ versus time, and line scan of $[Ca]_i$. The arrow in each case indicates the time when voltage clamp started. The parameters are the same as in Fig.1A in the main text but Ca overload ($[Ca]_o$=5 mM) with $[Na]_i$=10 mM and 7 mV left-shift in act_{ss} of $I_{Ca,L}$. **A**. The free-running voltage case in which repolarization failure occurs. **B**. Constant voltage clamp with normal LCCs present in CRUs. **C**. Same as B, but with a constant uniformly distributed $I_{Ca,L}$. **D**. Sinusoidal voltage clamp ($V(t)=A\sin 2\pi ft$ with A=20 mV and f=4 Hz) with normal LCCs present in CRUs. **E**. Same as D but with a constant uniformly distributed $I_{Ca,L}$. **F**. Voltage and $[Ca]_i$ versus time for a sinusoidal voltage clamp with normal LCCs present in CRUs, at different driving frequencies. Upper two panels: f=2 Hz. Lower two panels: f=1 Hz.

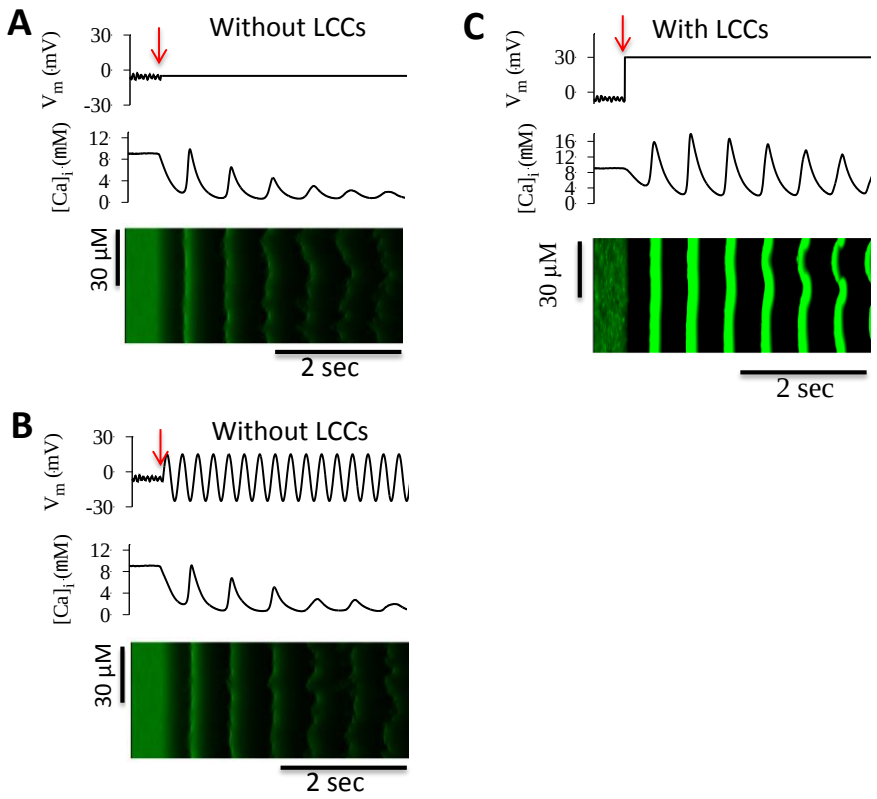

Fig.S8. Ca oscillations under different voltage clamp conditions (same as Fig.S7). **A** and **B**. The LCCs were removed without a constant Ca flux for compensation as in Fig.S7. Although the overall Ca decreased, the oscillations maintained. **C**. The LCCs were present, but the voltage was clamp at a higher value so that the LCCs are mostly inactivated to allow Ca oscillations to occur.

Interactions between voltage and Ca cycling during the long AP plateau (Detailed description of Figs.S7 and S8)

To explain the observation shown in the experiments in Fig.6 and the corresponding simulation in Fig.7 in the main text, in which no Ca oscillations (or very small fluctuations) in the long plateau phase but oscillations occur during the EAD phase, we carried out simulations (Figs.S7 and S8) by clamping the voltage during the AP plateau, so that we could observe the intrinsic underlying Ca cycling dynamics. We chose a parameter setting in which repolarization failure occurred such that voltage during the plateau remained around ~-5 mV, as illustrated in Fig.S7A. When no voltage clamp was imposed, voltage and whole-cell Ca exhibited small but irregular oscillations, and $[Ca]_i$ remained high. The line scan of Ca shows a random spatiotemporal pattern. We hypothesized that the random spatiotemporal pattern of Ca release under these conditions was likely to be related to the random openings of LCCs producing a random spatial pattern of Ca release sites during the plateau. To investigate how random opening of LCCs affects Ca oscillations, we carried out the following voltage clamp simulations. After starting each simulation from identical initial conditions, we imposed at a certain time point (arrow) either a voltage clamp to a constant voltage (Figs.S7B-C) or a voltage oscillation around the mean voltage (Figs.S7D-F).

When the voltage was held constant to promote random unsynchronized LCC openings, the whole-cell Ca and line scan (Fig.S7B) were very similar to the free-running case of repolarization failure (Fig.S7A). However, if LCCs were removed from the CRUs such that they could no longer trigger Ca sparks directly, and

were replaced by a uniformly-distributed constant Ca flux of the same magnitude as the LCC current so as to maintain the same cellular Ca level, a clear well-organized oscillation pattern immediately developed, as seen in the whole-cell Ca and the line scan (Fig.S7C). Even if the LCCs were removed without replacing them with a uniformly distributed constant Ca flux, Ca oscillations still developed immediately, but subsequently decreased in amplitude as the cellular Ca level declined due to the reduction in Ca entry (Fig.S8). Alternatively, if the voltage was held at a higher voltage to completely inactivate the LCCs, similar Ca oscillations occurred (Fig.S8).

If, instead of holding voltage constant during the plateau, a sinusoidal voltage clamp was imposed, the random spatiotemporal pattern of Ca sparks was replaced by a Ca oscillation pattern at the same frequency as the voltage oscillation (Fig.S7D), but with an alternating pattern. If the LCCs were removed and substituted by an equivalent constant Ca flux (Fig.S7E), however, the Ca oscillations did not alternate and exhibited an oscillation pattern virtually identical to that for the constant voltage case (Fig.S7C). However, now the periodic Ca oscillations were decoupled from the voltage oscillations, such that the frequencies of Ca and voltage oscillations were completely different. Fig.S6F shows $[Ca]_i$ for different oscillating frequencies of voltage with LCC intact (as in Fig.S7D). As the voltage oscillation frequency decreased, Ca alternans disappeared and $[Ca]_i$ developed a regular pattern (Fig.S7F, upper trace). However, if the driving frequency was decreased further, an alternating Ca oscillation pattern occurred again (Fig.S7F, lower trace).

These simulations demonstrate the following. When voltage is constant or nearly constant (Fig.S7B), the openings of the LCCs are random and uniform in space and time, resulting in random firings of CRUs in space and time. Therefore, at any time point, a spatially random portion of CRUs have yet to recover from their preceding firing. This random distribution of refractory CRUs reduces the likelihood that excitable CRUs activated by random openings of their LCCs or RyRs will be able to recruit neighboring CRUs and synchronize their refractory periods as required to generate an organized Ca oscillation. This is similar to the mechanism described in our previous study (2) showing that Ca waves and oscillations are emergent properties of the CRU network which strongly depend on CRU recruitment. On the other hand, when the LCCs are removed and replaced by an equivalent Ca flux (Fig. S7C), the number of randomly-firing CRUs causing dispersion of CRU refractoriness are reduced. This allows more effective recruitment to occur, which synchronizes the CRUs for organized Ca oscillations.

For the cases in which voltage oscillates (Figs. S7D-F), fewer LCCs are available for opening at high voltages but more are available at low voltages, and thus the voltage oscillation causes synchronous opening and closing of LCCs, resulting in synchronous firing of the CRUs, accounting for the organized Ca release patterns shown in Fig.S7D. However, if the driving frequency is fast so that the CRUs have not completely recovered from their previous firing, Ca alternans results, similar to the refractoriness mechanism of Ca alternans caused by rapid pacing with a free-running AP (16). When the driving frequency became slower so that CRUs had time to fully recover between oscillations, Ca alternans disappeared (Fig.S7F, upper traces). At even slower driving frequencies (Fig. S7F, lower traces), spontaneous synchronous CRU firings occurred between two pacing beats, resulting in a spontaneous beat followed by a voltage-driven beat, which is another type of Ca alternans.

References

1. Orth, P. M. R., J. C. Hesketh, C. K. H. Mak, Y. Yang, S. Lin, G. N. Beatch, A. M. Ezrin, and D. Fedida. 2006. RSD1235 blocks late INa and suppresses early afterdepolarizations and torsades de pointes induced by class III agents. Cardiovasc. Res. 70:486-496.
2. Nivala, M., C. Y. Ko, M. Nivala, J. N. Weiss, and Z. Qu. 2012. Criticality in intracellular calcium signaling in cardiac myocytes. Biophys. J. 102:2433-2442.
3. Liu, G. X., B. R. Choi, O. Ziv, W. Li, E. de Lange, Z. Qu, and G. Koren. 2012. Differential conditions for early after-depolarizations and triggered activity in cardiomyocytes derived from transgenic LQT1 and LQT2 rabbits. J. Physiol. 590:1171-1180.
4. Spencer, C. I., S. Baba, K. Nakamura, Ethan A. Hua, Marie A. F. Sears, C.-c. Fu, J. Zhang, S. Balijepalli, K. Tomoda, Y. Hayashi, P. Lizarraga, J. Wojciak, Melvin M. Scheinman, K. Aalto-Setälä, Jonathan C. Makielski, Craig T. January, Kevin E. Healy, Timothy J. Kamp, S. Yamanaka, and Bruce R. Conklin. 2014. Calcium Transients Closely Reflect Prolonged Action Potentials in iPSC Models of Inherited Cardiac Arrhythmia. Stem Cell Reports 3:269-281.
5. Morotti, S., A. G. Edwards, A. D. McCulloch, D. M. Bers, and E. Grandi. 2014. A novel computational model of mouse myocyte electrophysiology to assess the synergy between Na+ loading and CaMKII. J. Physiol. 592:1181-1197.
6. Goldhaber, J. I., L. H. Xie, T. Duong, C. Motter, K. Khuu, and J. N. Weiss. 2005. Action potential duration restitution and alternans in rabbit ventricular myocytes: the key role of intracellular calcium cycling. Circ. Res. 96:459-466.
7. Rae, J., K. Cooper, P. Gates, and M. Watsky. 1991. Low access resistance perforated patch recordings using amphotericin B. J. Neurosci. Methods 37:15-26.
8. Puisieux, F. L., M. M. Adamantidis, B. M. Dumotier, and B. A. Dupuis. 1996. Cisapride-induced prolongation of cardiac action potential and early afterdepolarizations in rabbit Purkinje fibres. Br. J. Pharmacol. 117:1377-1379.
9. Xie, L.-H., F. Chen, H. S. Karagueuzian, and J. N. Weiss. 2009. Oxidative Stress-Induced Afterdepolarizations and Calmodulin Kinase II Signaling. Circ. Res. 104:79-86.
10. Chang, M. G., C. Y. Chang, E. de Lange, L. Xu, B. O'Rourke, H. S. Karagueuzian, L. Tung, E. Marban, A. Garfinkel, J. N. Weiss, Z. Qu, and M. R. Abraham. 2012. Dynamics of Early Afterdepolarization-Mediated Triggered Activity in Cardiac Monolayers. Biophys. J. 102:2706-2714.
11. Collins, T. J. 2007. ImageJ for microscopy. BioTechniques 43:25-30.
12. Restrepo, J. G., J. N. Weiss, and A. Karma. 2008. Calsequestrin-mediated mechanism for cellular calcium transient alternans. Biophys. J. 95:3767-3789.
13. Luo, C. H., and Y. Rudy. 1994. A dynamical model of the cardiac ventricular action potential: I. simulations of ionic currents and concentration changes. Circ. Res. 74:1071-1096.
14. Rush, S., and H. Larsen. 1978. A practical algorithm for solving dynamic membrane equations. IEEE Trans. Biomed. Eng. 25:389-392.
15. Tian, T., and K. Burrage. 2004. Binomial leap methods for simulating stochastic chemical kinetics. J. Chem. Phys. 121:10356-10364.
16. Qu, Z., M. Nivala, and J. N. Weiss. 2013. Calcium alternans in cardiac myocytes: Order from disorder. J. Mol. Cell. Cardiol. 58:100-109.